Geoscience Frontiers 12 (2021) 101101

Contents lists available at ScienceDirect

Geoscience Frontiers

journal homepage: www.elsevier.com/locate/gsf

Research Paper

Element mapping the Merensky Reef of the Bushveld Complex

William Smith [a,*], Wolfgang Maier [a], Stephen Barnes [b], Gareth Moorhead [c], David Reid [d], Bartosz Karykowski [e]

[a] School of Earth and Ocean Sciences, Cardiff University, Cardiff CF240DE, United Kingdom
[b] CSIRO Mineral Resources, Perth 6160, Australia
[c] CSIRO, Clayton, Victoria, Australia
[d] University of Cape Town, South Africa
[e] Fugro Germany Land GmbH, 12555 Berlin, Germany

ARTICLE INFO

Article history:
Received 7 May 2020
Received in revised form 10 August 2020
Accepted 4 November 2020
Available online 03 December 2020

Handling Editor: Nick M W Roberts

Keywords:
Merensky Reef
Bushveld Complex
Magmatic sulphide
Platinum-group elements
PGE
Anorthosite

ABSTRACT

The Merensky Reef hosts one of the largest PGE resources globally. It has been exploited for nearly 100 years, yet its origin remains unresolved. In the present study, we characterised eight samples of the reef at four localities in the western Bushveld Complex using micro-X-ray fluorescence and field emission scanning electron microscopy. Our results indicate that the Merensky Reef formed through a range of diverse processes. Textures exhibited by chromite grains at the base of the reef are consistent with supercooling and *in situ* growth. The local thickening of the Merensky chromitite layers within troughs in the floor rocks is most readily explained by granular flow. Annealing and deformation textures in pyroxenes of the Merensky pegmatoid bear testament to recrystallisation and deformation. The footwall rocks to the reef contain disseminations of PGE rich sulphides as well as olivine grains with peritectic reaction rims along their upper margins suggesting reactive downward flow of silicate and sulphide melts. Olivine-hosted melt inclusions containing Cl-rich apatite, sodic plagioclase, and phlogopite suggest the presence of highly evolved, volatile-rich melts. Pervasive reverse zonation of cumulus plagioclase in the footwall of the reef indicates dissolution or partial melting of plagioclase, possibly triggered by flux of heat, acidic fluids, or hydrous melt. Together, these data suggest that the reef formed through a combination of magmatic, hydrodynamic and hydromagmatic processes.

1. Introduction

The Merensky Reef of the Bushveld Complex, South Africa, hosts one of the largest platinum-group element (PGE) resources in the world. It has been exploited for almost a century since its discovery by Hans Merensky in 1924 (Wagner, 1929). Renewed interest in its petrogenesis has arisen after the discovery of the Flatreef in the northern limb of the Bushveld Complex, which is interpreted to be an up-dip extension of the Merensky Reef (Grobler et al., 2019). Numerous lithological, petrological, and geochemical studies have been conducted on the reef, contributing to the assertion by Cox and Singer (1986) that magmatic Ni-Cu-PGE sulphide deposits are amongst the best understood on Earth. This assessment proved to be too optimistic as a consensus on the petrogenesis of the Merensky Reef remains as elusive as ever.

Notably, advances in analytical techniques have revealed added layers of complexity. For example, the geochronological work of Mungall et al. (2016) showed that the ages of zircon and baddeleyite grains in layers of the Rustenburg Layered Suite are out of sequence. Moreover, Abernethy (2019) showed that many of the CZ layers have multiple zircon populations, separated by as much as 500 kyr, which could reflect the presence of antecrysts, recrystallised in response to late sill intrusion and/or reactive porous flow. *In situ* trace element studies of silicate minerals (*e.g.*, Mathez et al., 1997; Arndt et al., 2005; Godel et al., 2011; Yang et al., 2013; Tanner et al., 2014; Karykowski et al., 2017) remain equally difficult to interpret due to effects of trapped melt crystallisation likely resulting in extreme incompatible trace element enrichment, zonation and the crystallisation of incompatible trace element-enriched phases with which the major silicates subsequently could have undergone diffusive exchange. These problems highlight the challenges of unravelling the origin of slowly cooling cumulate rocks that are exposed to prolonged flux of heat, melts and volatiles, triggering post-magmatic diffusion and textural equilibration.

We argue that one of the main reasons for the gaps in understanding is the scarcity of studies that link microscopic and macroscopic observations. The present study provides detailed element maps of several dm-sized samples of the Merensky Reef (MR) from four localities in the western Bushveld Complex (WBC) using the Maia Mapper micro-X-ray fluorescence (μXRF) and field emission scanning electron microscopy (FESEM).

* Corresponding author.
E-mail address: smithwd1@cardiff.ac.uk (W. Smith).

https://doi.org/10.1016/j.gsf.2020.11.001

2. Geological overview of the Bushveld Complex

The Rustenburg Layered Suite (RLS) of the Bushveld Complex (~ 2.055 Ga; Scoates and Wall, 2015; Fig. 1) forms the most extensive and voluminous layered mafic-ultramafic intrusive suite on Earth, outcropping and sub-cropping over at least 60,000 km^2 (Eales and Cawthorn, 1996). The RLS consists of an ~6–8 km package of cumulates that host the majority of the world's PGE, Cr, and V resources, as well as significant Ni and Cu resources (Cawthorn, 2015).

The RLS is divided into five stratigraphic units, including the Marginal, Lower, Critical, Main, and Upper zones (Hall, 1924). The bulk of the PGE, Ni, Cu, and Cr mineralisation is located in the Critical Zone (CZ) which is sub-divided into a predominantly orthopyroxenitic lower sub-zone (CZL) and an interlayered upper sub-zone (CZ_U), the latter being characterised by so-called cyclic units typically consisting of a basal chromitite layer overlain by pyroxenite (or rarely harzburgite), norite and anorthosite (Eales et al., 1986). Enrichments of PGE are found towards the base of many of the cyclic units and in a few cases can form economically important reefs, notably the world's two largest PGE repositories, the UG2 chromitite and the MR. These stratiform reefs can be traced along much of the strike of the western and eastern lobes, and in part of the northern lobe, of the Bushveld Complex, *i.e.,* for several 100 km (Cawthorn, 2015; Grobler et al., 2019).

3. The Merensky Reef

3.1. Stratigraphy

In the WBC the MR occurs at the base of the Merensky Cyclic Unit (MCU; Wagner, 1929; Vermaak, 1976; Leeb-Du Toit, 1986; Naldrett et al., 1986; Viljoen and Hieber, 1986; Ballhaus et al., 1988; Eales et al., 1988, 1990). At most localities, the footwall rocks to the MCU consist of norite and anorthosite. The typical stratigraphy of the MCU comprises a basal chromitite stringer (several mm to cm in thickness), which is overlain by a pyroxenitic or harzburgitic pegmatoidal layer several cm to >1 m thick, a second chromitite stringer, several metres of medium-grained pyroxenite, a few meters of norite and several cm of anorthosite before the next cyclic unit, *i.e.,* the Bastard unit, follows. Sulphides enriched in PGE, Ni and Cu are typically found in the chromitite stringers, the pegmatoid and the lower few cm to decimetres of the pyroxenite. In many cases, sulphides also occur in the uppermost few cm to dm (and sometimes meters) of the footwall anorthosite (Leeb-Du Toit, 1986; Barnes and Maier, 2002; Naldrett et al., 2009; Hutchinson et al., 2015; Mitchell et al., 2019). The thickness of the mineralised interval remains broadly constant along much of the exposed strike (with the exception of the southwestern portion of the WBC where it thickens to up to ~10 m, and in the northern lobe where proposed Merensky Reef correlatives reach several 10s of m in thickness; Grobler et al., 2019), as do the metal grades and compositions of the base metal sulphides and

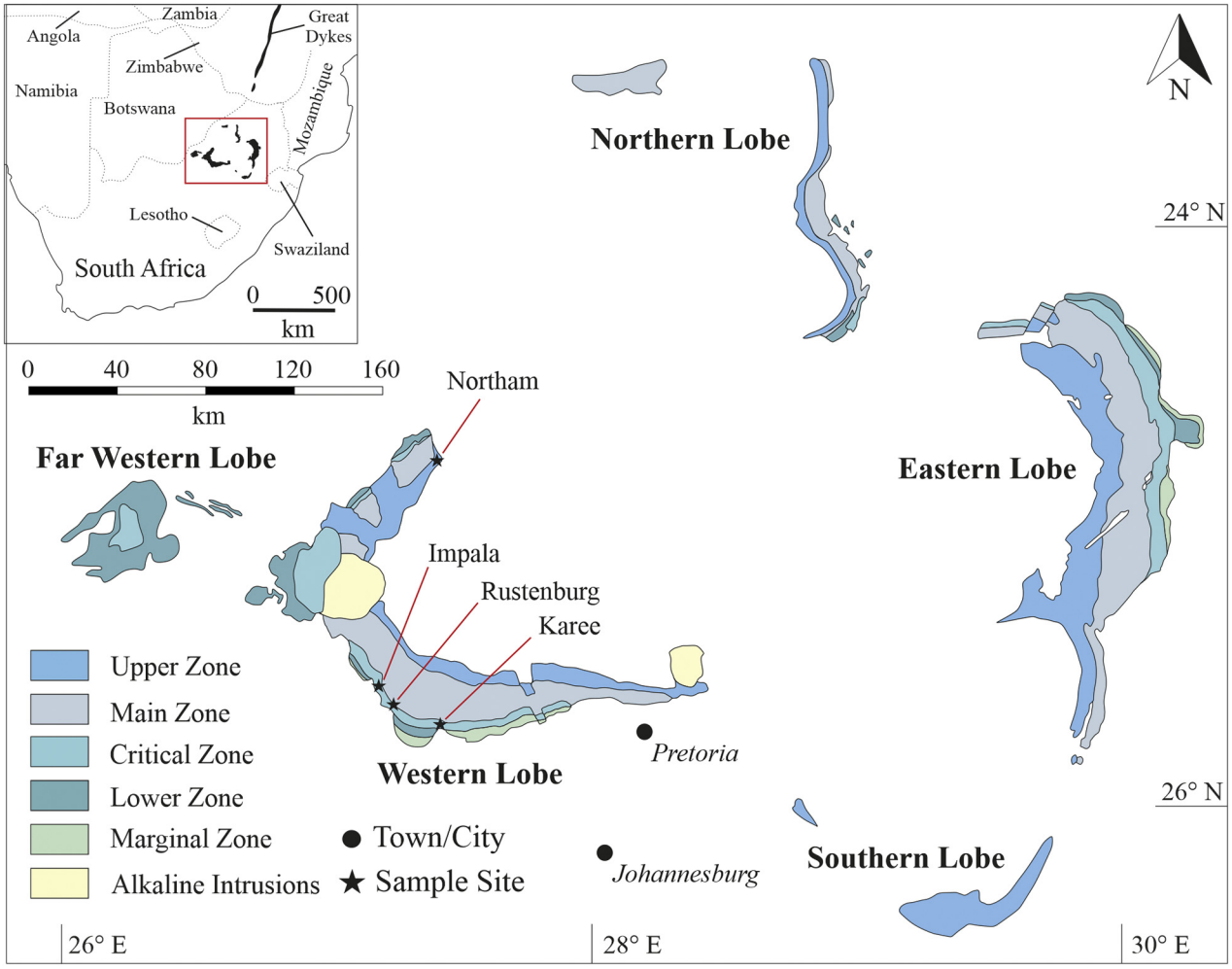

Fig. 1. Geological map of the Bushveld Complex (modified from Mungall et al., 2016), showing sample locations.

platinum-group minerals (Cawthorn, 2015; Naldrett et al., 2009). Lateral variations in the stratigraphy of the reef and its footwall and hanging wall have been interpreted to be controlled mainly by distance to a putative feeder zone near Union Section (Eales et al., 1988). Thus, in the proximal facies (at Union Section), the Merensky pegmatoid is thicker and contains more olivine than in the relatively more distal facies to the northeast (*e.g.,* at Amandelbult and Northam mines), and southeast of Union (*e.g.,* at the Impala, Rustenburg, and Karee mines). In the most distal facies (to the east of Marikana) the reef splits into two layers separated by up to 10 m of barren pyroxenite. In contrast, the footwall rocks of the reef are thinnest at Union and become progressively thicker to the northeast and southeast (Eales et al., 1988; Maier and Teigler, 1995; Maier and Eales, 1997).

In addition to the regional stratigraphic changes, localised variation in reef stratigraphy is observed in so-called potholes where the reef cuts across the footwall rocks in a transgressive manner (Schmidt, 1952; Barry, 1964; Buntin et al., 1985; Campbell, 1986; Ballhaus et al., 1988; Eales et al., 1988; Viljoen, 1999). Potholes tend to be elliptical in plan view, ranging from a few cm to 100 s of metres in diameter and up to 100 m in depth (Viljoen, 1999), being particularly deep where the footwall rocks are leucocratic (*e.g.,* anorthositic or leuconoritic). Centimetre- to dm-scale apophyses may protrude laterally from the potholes into the surrounding lithologies (Ballhaus et al., 1988; Latypov et al., 2017; Mitchell et al., 2019). The apophyses have thicknesses between a few cm to more than a meter and are up to >100 m long. The origin of potholes has been ascribed to three main models: (i) thermo-chemical (and/or thermo-mechanical) erosion of the footwall (Schmidt, 1952; Irvine et al., 1983; Campbell, 1986; Eales et al., 1988; Latypov et al., 2017), (2) cumulate resorption and/or non-deposition in response to volatile fluxing of the compacting cumulate pile (Barry, 1964; Von Gruenewaldt, 1979; Kinloch, 1982; Buntin et al., 1985; Ballhaus et al., 1988; Boudreau, 1992; Boudreau and McCallum, 1992) and (3) deposition of cumulates into extensional pull-apart structures (Carr et al., 1999; Maier et al., 2016). The distribution of potholes in the WBC has been summarised in Viljoen (1999). In the Rustenburg area 15%–30% of the reef occurs in potholes. In the northwestern Bushveld (*i.e.,* at Union, Amandelbult and Northam mines), the reef resembles that in the Rustenburg area, but its total thickness (including that of the pegmatoid) is greater and the potholes are deeper. The nature of the MR shows considerable differences depending on its position within the potholes. At the transition from normal to potholed reef (*i.e.,* so called "contact reef"), the chromitite stringers tend to become thin and converge to form a single layer while the intermittent pegmatoid pinches out. At the base of large potholes ("regional pothole reef"), the thickness of the chromite stringer and the pegmatoid tend to be highly irregular, but the PGE grade tends to be elevated.

In the present work, we studied examples of normal (non-potholed) reef at Rustenburg and Karee mines, contact reef with a single basal chromite stringer of enhanced thickness at Impala mine, and regional pothole reef with or without pegmatoid and mostly lacking a well-defined chromitite stringer at Northam mine.

3.2. Overview of main petrogenetic models

The MR has been studied for almost a century and thus it is no surprise that numerous theories have been proposed to explain its origin:

(1) Gravitational settling of sulphide melt that exsolved from silicate magma upon replenishment of the magma chamber and consequent mixing between resident and replenishing magmas (Campbell et al., 1983). The turbulence associated with chamber replenishment caused the high *R* factors proposed to be required to achieve the extremely high PGE tenor of the sulphides (up to ~1000 ppm; Barnes and Maier, 2002; Naldrett et al., 2009). Dense chromite crystals and immiscible sulphide liquid settled through the magma column and accumulated on the temporary floor of the magma chamber.

(2) Introduction of chalcophile metals to a volatile-undersaturated cumulate horizon by ascending Cl-rich magmatic fluids (Ballhaus and Stumpfl, 1986). Boudreau (1986,2008) proposed that all six PGE, Ni, and Cu were transported by the fluids, which has remained highly controversial amongst most other researchers.

(3) Recrystallisation of a primary magmatic, sulphide-bearing proto-reef triggered by ascending fluids (Nicholson and Mathez, 1991; Mathez and Kinzler, 2017). Magmatic vapour expelled during the crystallisation of the floor rocks to the reef was trapped in the incompletely solidified pyroxenitic proto reef. The fluids triggered melting of orthopyroxene, thereby transforming the footwall norite to anorthosite, while stabilising chromite and olivine in the pyroxenite. The fluids were also responsible for the pegmatoidal textures of the reef, and the presence of graphite and phlogopite (Ballhaus et al., 1986).

(4) Intrusion of sulphide and/or PGE enriched magma(s) onto (or into) a pre-existing cumulate pile (Lee and Butcher, 1990; Lee, 1996; Mitchell and Scoon, 2007; Naldrett et al., 2009; Mungall et al., 2016). Important lines or evidence cited include sharp contacts between, and bifurcations of layers, and out-of-sequence zircon ages. However, Karykowski et al. (2017) have presented evidence for reactive porous flow and Abernethy (2019) argued this process could explain the highly complex geochronological data from the reef interval.

(5) *In situ* crystallisation of chromite and sulphide at the crystal-liquid interface (Eales and Reynolds, 1986; Vukmanovic et al., 2013; Latypov et al., 2015, 2017, 2020; Chistyakova et al., 2019). Superheated, but sulphide melt saturated magma eroded and partially melted the feldspathic floor of the reef, thereby causing saturation in, and crystallisation of chromite at the floor of the magma chamber. The co-precipitating sulphides became enriched in PGE when chalcophile-undepleted magma convected along the floor of the chamber (Latypov et al., 2017).

(6) Hydrodynamic sorting of silicates, oxides, and sulphides during the slumping of crystal slurries triggered by chamber subsidence and associated seismic activity (Maier et al., 2013).

4. Materials and methods

Samples of the MR were acquired from four operational mines in the WBC (Northam, Impala, Rustenburg, and Karee; Fig. 1). Polished thin sections (~ 30 μm; RPM-2 and Karee) and cut slabs (RPM-1, Impala, and Northam) were imaged and scanned prior to element mapping. High-resolution element maps were produced at Cardiff University using a Zeiss Sigma HD Analytical Field Emission Gun Scanning Electron Microscope equipped with two Oxford Instruments 150 mm^2 energy dispersive spectrometers. Element maps generated using this method represent high-resolution qualitative compositional maps of sample sections that provide an insight into modal mineralogy, mineral composition and zonation, and microtextures. All element maps were produced using an accelerating voltage of 20 kV and livetime of 1 s at a working distance of 8.9 mm. Beam current drift was optimised using a pure cobalt standard between element maps. Magnification and pixel dwell time were selected upon required feature (entire sections or fine-scale oscillatory zoning). Data were processed in Aztec Software, within which modal mineralogy was computed.

Qualitative element distribution maps were acquired as CSIRO, Melbourne, Australia, using the Maia Mapper, a high definition μXRF element mapping system developed for efficient element mapping of polished rock slabs (Ryan et al., 2018). The Maia Mapper comprises: (i) a Maia 384-element X-ray detector; (Kirkham et al., 2010); (ii) a high-brightness MetalJet D2 liquid metal micro-focus X-ray source from Excillum (Larsson et al., 2011); (iii) a polycapillary X-ray lens,

producing a focus on a ~ 30 μm target (see xos.com); and (iv) a high-precision, high-speed sample positioning mechanical system that presents samples up to 500 mm × 150 mm in size and 10 kg in weight. Data are acquired continuously as individual photon events tagged with a sensor number and X-Y position. Image 'pixels' are reconstructed from the X-Y position, with an effective dwell time in each pixel set by the motion velocity. Data reduction is performed using GeoPIXE™ software (Ryan et al., 2010), which uses a standardless fundamental parameter method. The data is then analysed event-by-event using the dynamic analysis method for real-time spectrum deconvolution to accumulate element concentration maps with spectral overlap, pileup, and background removed (Ryan et al., 2014).

In situ Sr isotope ratios of plagioclase were determined across six thin sections from a drill-core specimen (~ 16.8 cm in length) from Karee, using a Photo Machine Analyte G2 laser microprobe coupled to a nu Plasma HR MC-ICP-MS system at the Geological Survey of Finland, Espoo. Analytical instrumentation and parameters are the same as those described in Karykowski et al. (2017). The standards and data are reported in Supplementary Material 1.

5. Results

5.1. Merensky Reef at the Rustenburg platinum mine

5.1.1. Sample RPM-1

Sample RPM-1 is a polished slab measuring ~30 cm in height, ~ 10 cm in width, and ~ 2 cm in thickness (Table 1). Both sides of the sample were imaged on the Maia Mapper μXRF and show remarkable lithological variability considering the ~1.5 cm thickness of the sample (Figs. 2–4).

5.1.1.1. Footwall norite. The rock is faintly layered and comprises subcotectic proportions of anhedral orthopyroxene (~ 30%–32%) and plagioclase (~ 65%–75%). Plagioclase forms <0.6 mm subhedral grains, which display faint reverse compositional zoning. Orthopyroxene grains display anhedral but equant core zones (~ 1–4 mm) and extensive interstitial overgrowths (< 4 mm), which enclose abundant millimetric rounded plagioclase inclusions. Similar features have been previously described in Maier and Eales (1997), who showed that the inclusions tend to be slightly more calcic than the matrix plagioclase. Poikilitic clinopyroxene is a minor phase (< 5%). Chromite and phlogopite are not observed. Rare disseminations of very fine-grained base metal sulphides (po-pn-cp) occur in the upper portion of the rock and are mainly associated with plagioclase.

5.1.1.2. Footwall anorthosite. The rock forms the immediate footwall to the MR and has a thickness of ~3–5 cm. The contact to the underlying norite is sharp and undulating, forming pothole-like transgressions. Anorthosite enclaves in the upper portion of the footwall norite are interpreted to represent the 2D expression of anorthosite apophyses. The contact between the anorthosite layer and the overlying lower chromitite stringer of the MR is knife-sharp, but also highly irregular, resulting in the variable thickness of the anorthosite; a feature typical of the MR in the WBC (Viljoen et al., 1986; Eales et al., 1988). Plagioclase forms subhedral grains (0.3–0.7 mm in length) that are weakly aligned sub-parallel to the layering and show faint reverse zoning with relatively calcic rims. Notably, several traverses across the interval from norite to the MR showed no resolvable Ca-enrichment of plagioclase in the anorthosite relative to the underlying norite, contrary to the MR profile analysed by Naldrett et al. (1987). Interstitial clinopyroxene occurs in the uppermost 2 cm of the anorthosite and in the pothole-like transgressions in footwall norite. No chromite or phlogopite is observed within this unit, but the rock contains abundant fine-grained sulphides forming patchy composite disseminations of pyrrhotite (~ 64.0%), pentlandite (~ 21.2%), and chalcopyrite (~ 14.8%; Fig. 4). The sulphides are clearly concentrated in clinopyroxene-enriched domains, including the pothole-like transgressions in footwall norite, whereas anorthosite adcumulate domains are almost entirely free of sulphide. There are also abundant platinum-group minerals (PGMs) that occur almost exclusively in the periphery of base metal sulphides.

5.1.1.3. Lower chromitite. The lower chromitite stringer, forming the base of the MCU, is ~1–3 cm thick, and has sharp basal and upper contacts. The chromitite stringer is progressively thickening where the reef begins to transgress into the footwall anorthosite, with the exception of the finger-like pothole that is enveloped by a mere 1–3 mm selvage of chromitite. The bulk of the chromitite layer (~ 68%) is made up of chromite grains many of which show amoeboidal textures (Fig. 2; Supplementary Fig. 1). In addition, there are abundant vermiform grains, particularly near the base of the layer. The matrix to the chromite consists predominantly of interstitial plagioclase (~ 87%) and subordinate clinopyroxene (< 3.3%), which forms up to ~2 cm anhedral oikocrysts. Along the upper margin of the chromitite layer, the matrix consists largely of orthopyroxene, hosting small micrometric chromite grains. In addition, the chromitite layer contains fine-grained (< 0.3 mm) phlogopite (< 0.5%), which is almost always associated with fine-grained base metal sulphides (Supplementary Fig. 2).

5.1.1.4. Pegmatoid. The pegmatoid shows considerable variability in thickness. In face A of the sample, the thickness of the pegmatoid varies from 0 to 10 cm, where the thickest portion directly overlies the

Table 1
Brief description of samples analysed for this study.

Sample ID	Location	Sampled lithotypes[a]	Length (cm)	Description	Figures
RPM-1	Rustenburg	FN → FA → LC → CP → UC → Px	~ 35	Mapped on both sides of the sample (see text), this sample extends from the FN to the Px. The FA shares a sharp, undulating contact with the LC. Two chromitite layers are defined on side (B) yet appear connected on side (A).	2, 3, 4 Supplementary Figs. 1 and 2
RPM-2	Rustenburg	FN → FA → LC → CP	~ 16	FN and FA overlain by a thin LC, which shares a sharp, undulating contact with the overlying CP.	5
IMP-BT	Impala	FN → FA → LC	~ 13	Reversely-zoned plagioclase in the FA immediately below the LC. Sulphide-phlogopite pairs occur distributed throughout the LC.	6
KR-1	Karee	FA → LC → CPx	~17	FA overlain by a thin LC and a thick coarse-grained pyroxenite, rich in base metal sulphides.	7
NTH-48c	Northam	FN → Px → FN → FA → LC	~ 11	Chromitite with footwall anorthosite and norite. The footwall contains a 5-cm-thick pyroxenite stringer.	8
NTH-10b	Northam	FON	~ 5	Footwall olivine norite situated below the non-pegmatoidal reef	9
NTH047	Northam	FON → FA	~ 7	FN and FA, deficient in chromite and base metal sulphides.	10
NTH-4612	Northam	FON → CPx + Cr	~ 18	FN overlain by coarse-grained pyroxenite, which hosts pods and stringers of chromite (+ base metal sulphides).	11

[a] FN = footwall norite, FON = footwall olivine norite, FA = footwall anorthosite, LC = lower chromitite, CP = central pegmatoid, CPx = central pyroxenite, UC = upper chromitite, Px = pyroxenite.

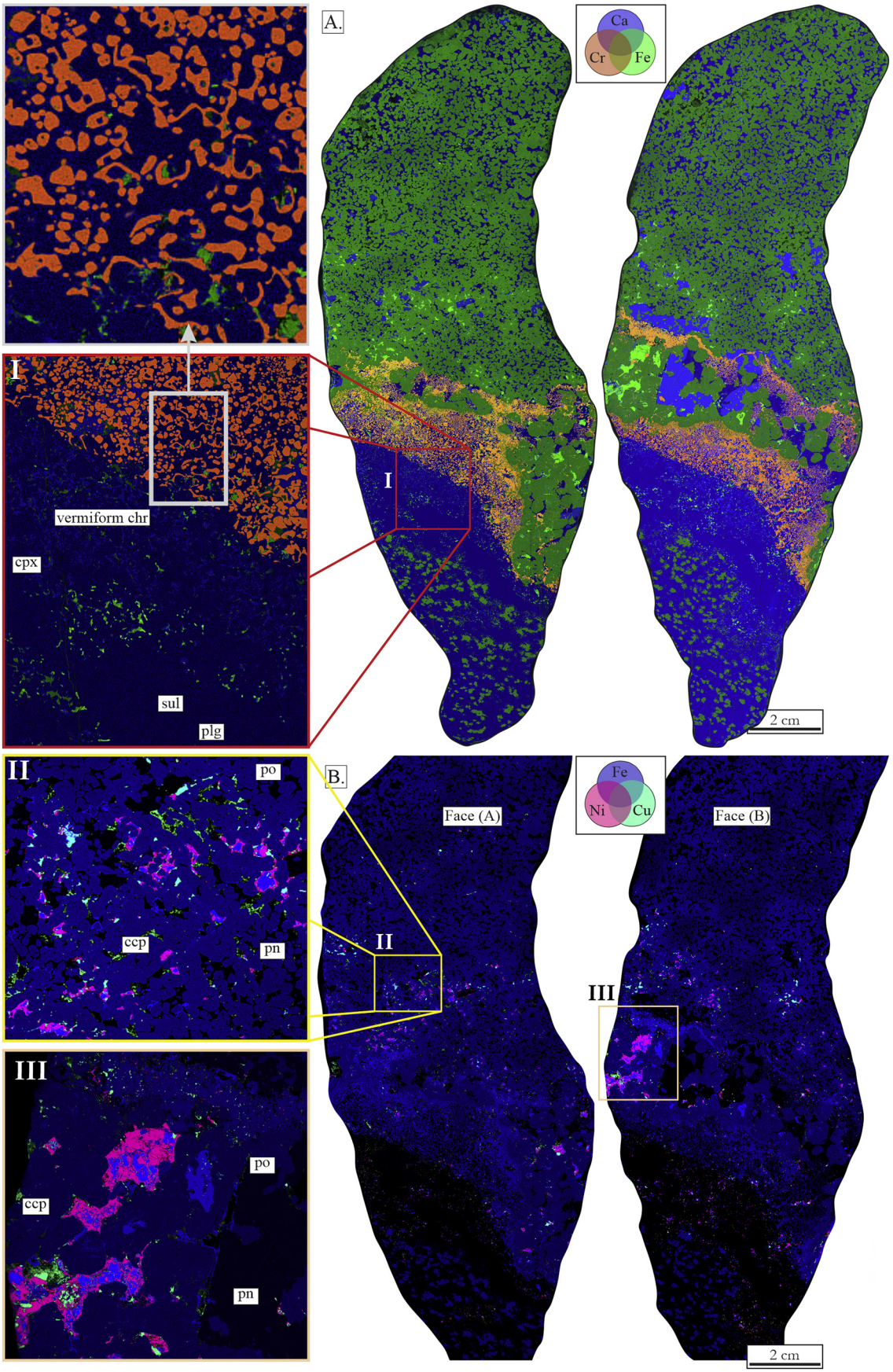
A.
Ca
Cr
Fe
I
vermiform chr
cpx
sul
plg
2 cm
II
po
ccp
pn
B.
Face (A)
Face (B)
Fe
Ni
Cu
III
2 cm

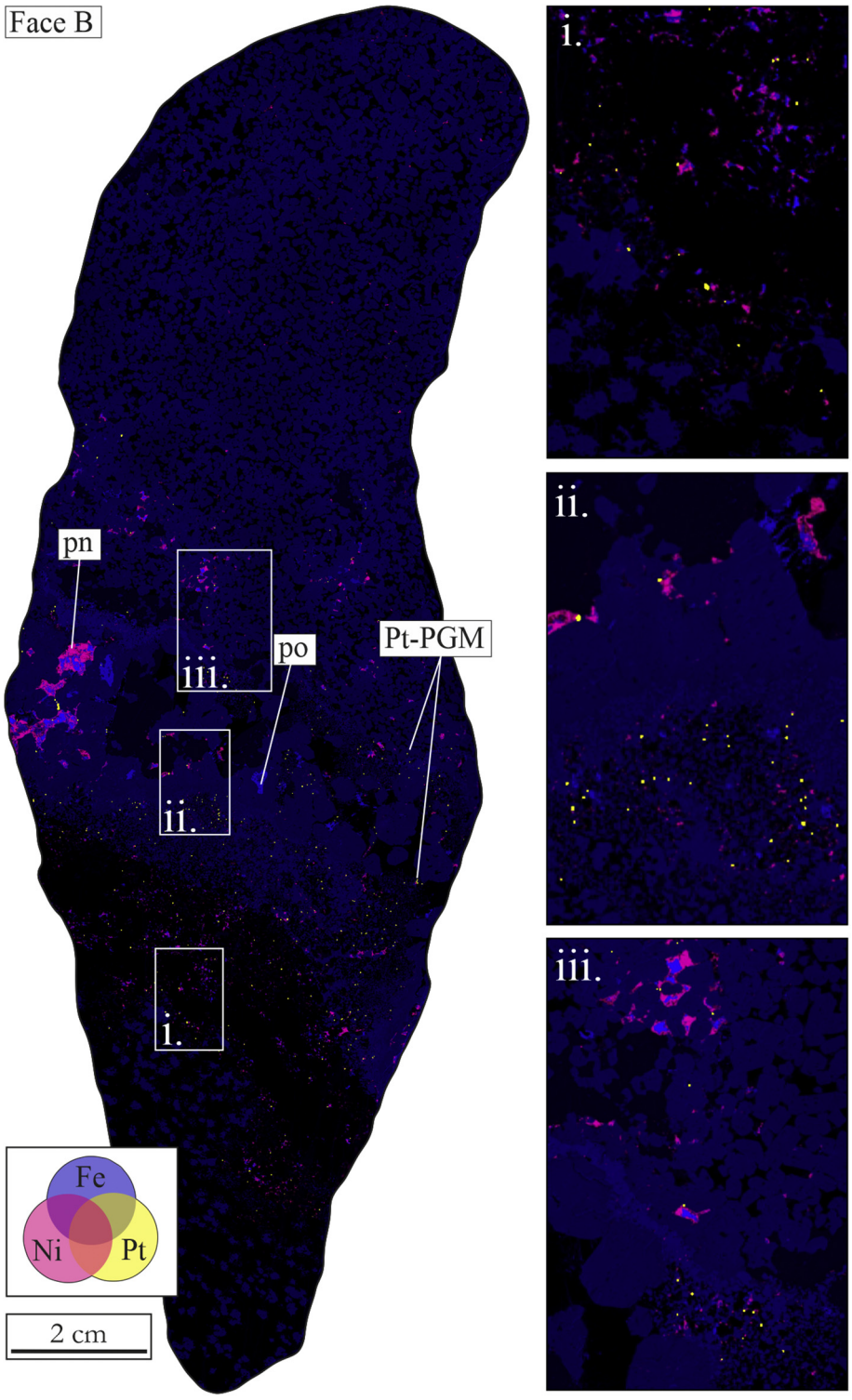

Fig. 3. μXRF Fe—Ni element map superimposed by a segmented Pt-PGM map of face (B) of sample RPM-1. Pt-minerals have been highlighted throughout the sample and shown in greater detail in the footwall anorthosite-norite (i), the lower chromitite (ii), and the upper chromitite-pyroxenite (iii). Note the abundance of Pt-phases at, or close to the margins of base metal sulphides. The footwall norite and pyroxenite are largely devoid of Pt-minerals.

thinnest portions of the basal chromitite and footwall anorthosite. In face B the pegmatoid shows less pronounced variation in thickness (~2–5 cm), but there is again a negative correlation between the thickness of the pegmatoid and that of the basal chromite stringer, *i.e.*, the thicker the chromite stringer, the thinner the pegmatoid. The pegmatoid consists mainly (~50%–70%) of coarse-grained (~2–7 mm in diameter),

Fig. 2. (A) μXRF Ca-Cr-Fe element map of face (A) and (B) of sample RPM-1. Observe the variability of the chromite and central pegmatoid in this sample. We observe vermiform chromite along the lower contact with the footwall anorthosite. (B) μXRF Fe-Ni-Cu element map of face (A) and (B) of sample RPM-1. Fairly equal proportions of base metal sulphides are observed in each horizon (see Fig. 4). Pentlandite generally lines the exterior of interstitial pyrrhotite. Supplementary Fig. 1 shows the prevalence of phlogopite throughout the whole sample and the occurrence of rutile in the chromitite seams. Plg = plagioclase, opx = orthopyroxene, cpx = clinopyroxene, sul = sulphide, chr = chromite, po = pyrrhotite, pn = pentlandite, ccp = chalcopyrite.

subhedral or anhedral orthopyroxene that displays convex-up undulations (few cm in amplitude) with the bracketing chromite stringers. Additional phases are anhedral, interstitial plagioclase (~21%), anhedral poikilitic clinopyroxene (~4.7%), and interstitial base metal sulphides (~1.5%). In much of the pegmatoid, chromite is relatively rare, with the exception of interstitial plagioclase that may contain abundant chromite grains that seemingly sunk downwards from the upper chromite stringer. Traces of interstitial quartz and fine-grained phlogopite (≤ 1%) occur throughout the layer, often spatially associated with base metal sulphides.

Base metal sulphides in the pegmatoid consist predominantly of pyrrhotite (~ 53.7%), with somewhat lower proportions of pentlandite (~ 29.4%) and chalcopyrite (~ 16.9%). Most sulphides are much coarser grained than in the lower and upper chromitite stringers, forming rounded or angular composite grains of up to 6 mm in diameter, but thin sulphide selvages along grain boundaries of silicates also occur. The sulphides tend to be spatially associated with orthopyroxene, whereas most plagioclase and clinopyroxene tend to host few sulphides.

5.1.1.5. Upper chromitite. The upper chromite stringer is much thinner (0–1 cm) and less continuous than the lower chromite stringer. The chromite grains are generally subhedral or anhedral and are annealed in places. Their grain size is highly variable (< 0.1–1 cm), resulting in distinct domains of relatively small and relatively large grains. The majority of chromite grains are hosted in intercumulus plagioclase and locally line the exterior margins of subhedral orthopyroxene grains. Few (< 2%) small phlogopite and rutile crystals occur amongst the chromite and intercumulus plagioclase (Supplementary Fig. 2). The upper contact of the stringer with medium grained pyroxenite tends to be sharp, but with closely spaced asymmetric undulations. The lower contact of the stringer with the Merensky pegmatoid tends to be more diffuse and irregular, with numerous fine chromite grains locally occurring in the pegmatoid.

5.1.1.6. Medium-grained pyroxenite. The upper portion of the MR is composed of medium-grained orthopyroxenite consisting mainly of subhedral orthopyroxene (~66%) and interstitial plagioclase (~32%), the latter forming centimetric oikocrysts. Orthopyroxenes hosted by plagioclase oikocrysts are typically more Cr-rich (expressed by darker green colours in Fig. 2) and less clustered than orthopyroxene outside the oikocrysts. With increasing proximity to the underlying upper chromitite stringer, the amount of intercumulus plagioclase decreases at the expense of sulphides. Clinopyroxene (< 9 mm) makes up ~6.8% of the rock and is more prevalent on face B where it constitutes up to ~10% of the lowermost few cm of the rock, including a large elongated clinopyroxene oikocryst hosting numerous small rounded orthopyroxene inclusions directly above the upper chromite stringer. Most clinopyroxene grains are subhedral oikocrysts comprising small (1–3 mm) inclusions of orthopyroxene. However, in face A there is one elongated subhedral grain. Phlogopite and quartz occur throughout the rock as minor accessory phases (< 1%). Phlogopite forms discrete anhedral to bladed crystals located interstitially to the pyroxene-plagioclase framework. The rock contains exceedingly little chromite (< 0.1%), and the identified grains are extremely small (< 10 μm) and occur with intercumulus plagioclase. This is remarkable in view of the fact that the pyroxenite is in direct contact with the upper Merensky Reef chromite layer.

Sulphides are concentrated in the lowermost 5 cm of the pyroxenite where they are predominantly associated with orthopyroxene, whereas the plagioclase and oikocrystic clinopyroxene are free of sulphides. Pyrrhotite is the most abundant sulphide (~ 40.7%), followed by pentlandite (~ 33.6%) and chalcopyrite (~ 25.7%; Fig. 4). Pentlandite typically rims pyrrhotite whereas chalcopyrite predominantly rims the silicate minerals. PGMs are abundant and always occur peripheral to the base metal sulphides (Fig. 3).

5.1.2. Sample RPM-2

Sample RPM-2 was cut to produce three thin sections that span the interval from the footwall norite across the anorthosite, lower chromite stringer and into the Merensky pegmatoid, each of which were mapped *via* SEM-EDS (Table 1; Fig. 5).

5.1.2.1. Footwall norite. The norite displays broadly cotectic proportions of orthopyroxene (~40%) and plagioclase (~60%). Plagioclase is up to 2.2 mm in diameter and forms mostly subhedral crystals. There is no clear evidence that the grains are compositionally zoned. Orthopyroxene forms anhedral grains with intercumulus overgrowths of up to ~2 mm. The grains contain rounded and sub-rounded inclusions (~ 0.3–1.2 mm) of plagioclase. Most of the inclusions are concentrated near the margins of the orthopyroxene. Rare fine-grained chromite crystals occur exclusively within the orthopyroxene overgrowths. Traces of phlogopite (< 0.1%) are present throughout the rock, except for the centres of orthopyroxene grains. Rare interstitial clinopyroxene occurs amongst the orthopyroxene overgrowths. Traces of base metal sulphides are present between plagioclase grains and within intercumulus orthopyroxene.

5.1.2.2. Footwall anorthosite. This layer measures ~5–6 cm in thickness and comprises domains of almost pure plagioclase, but also domains rich in intercumulus clinopyroxene. Although not quantitatively analysed, plagioclase shows relatively calcic rims. Clinopyroxene forms large (< 1.5 cm^2) oikocrysts, *e.g.,* in the immediate footwall of the MR. In addition, in the lower half of the anorthosite there is a ~ 0.5 cm-thick sub-horizontal layer enriched in intercumulus clinopyroxene, which also hosts abundant very fine-grained sulphides. In contrast, the remainder of the anorthosite lacks sulphides, with the exception of a few grains directly below the reef. No chromite is

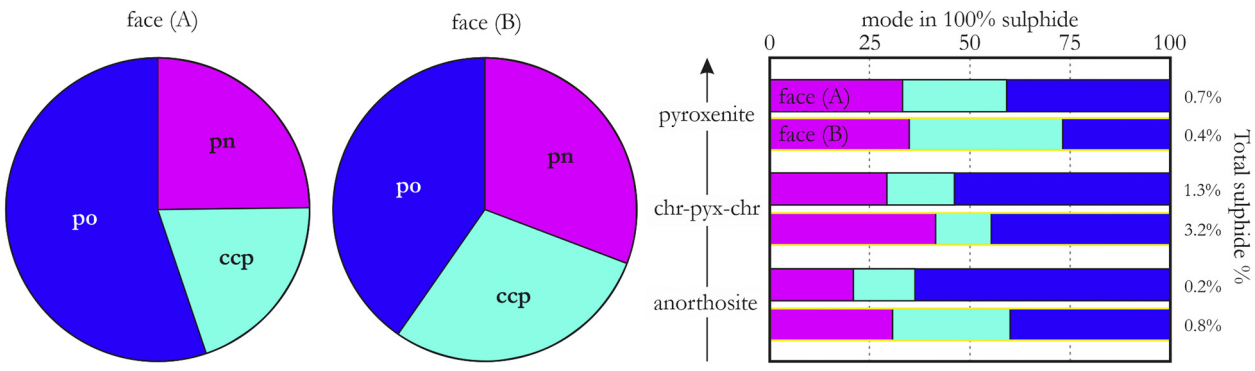

Fig. 4. Base metal sulphide modal abundances produced in GeoPIXE software for face (A) and (B) of sample RPM-1. Note that the anorthosite generally hosts higher relative proportions of pyrrhotite compared to the pyroxenite.

observed in the rock, but small amounts of phlogopite (~ 0.4%) occur interstitially to plagioclase. The largest grains of phlogopite (< 3 mm) are observed in close proximity to base metal sulphides. The contact with the underlying norite is less well defined than in sample RPM-1, but the contact with the overlying lower chromitite layer of the Merensky Reef is sharp, fairly regular, and marked by a relative enrichment in phlogopite (± rutile).

5.1.2.3. Lower chromitite. The layer has a constant thickness (~ 1.5 cm). Chromite grains display amoeboidal and annealed textures. Abundant sub-rounded inclusions of plagioclase and orthopyroxene represent matrix material that is exposed due to the irregular shape of the chromite crystals. Vermiform crystals as observed in sample RPM-1 are rare. The upper contact with the Merensky pegmatoid is sharp and displays ~5 mm wide concave undulations as well as a rind of fine-grained chromite, somewhat analogous to sample RPM-1. Plagioclase (~ 31%) is the primary matrix mineral, which forms an inter-connected network throughout the layer. Anhedral, oikocrystic orthopyroxene forms ~7.2% of the matrix and coats some of the chromite grains. Phlogopite (~ 0.8%) mostly occurs interstitial to chromite and tends to be spatially associated with base metal sulphides. The latter are found throughout the layer (~ 0.8%) and consist of po (~ 8.3%), pn (~ 42.2%), and ccp (49.5%). Most are located interstitial to chromite, but in some cases, they form inclusions within chromite.

5.1.2.4. Pegmatoid. The rock comprises the remainder of the sample (> 3 cm) and consists primarily of coarse-grained (< 2 cm) olivine (~ 41%), anhedral orthopyroxene (~ 22%) and interstitial plagioclase (~ 33%). The contact with the lower chromitite layer is characterised by a narrow (~ 1.5–1.8 mm) 'rim' of orthopyroxene and by ~1 cm wide undulations resembling load cast structures. Interstitial plagioclase is often rimmed by orthopyroxene. Chromite (~1.3%) mostly occurs as fine, anhedral or subhedral inclusions in orthopyroxene and sometimes plagioclase. Phlogopite occurs throughout the

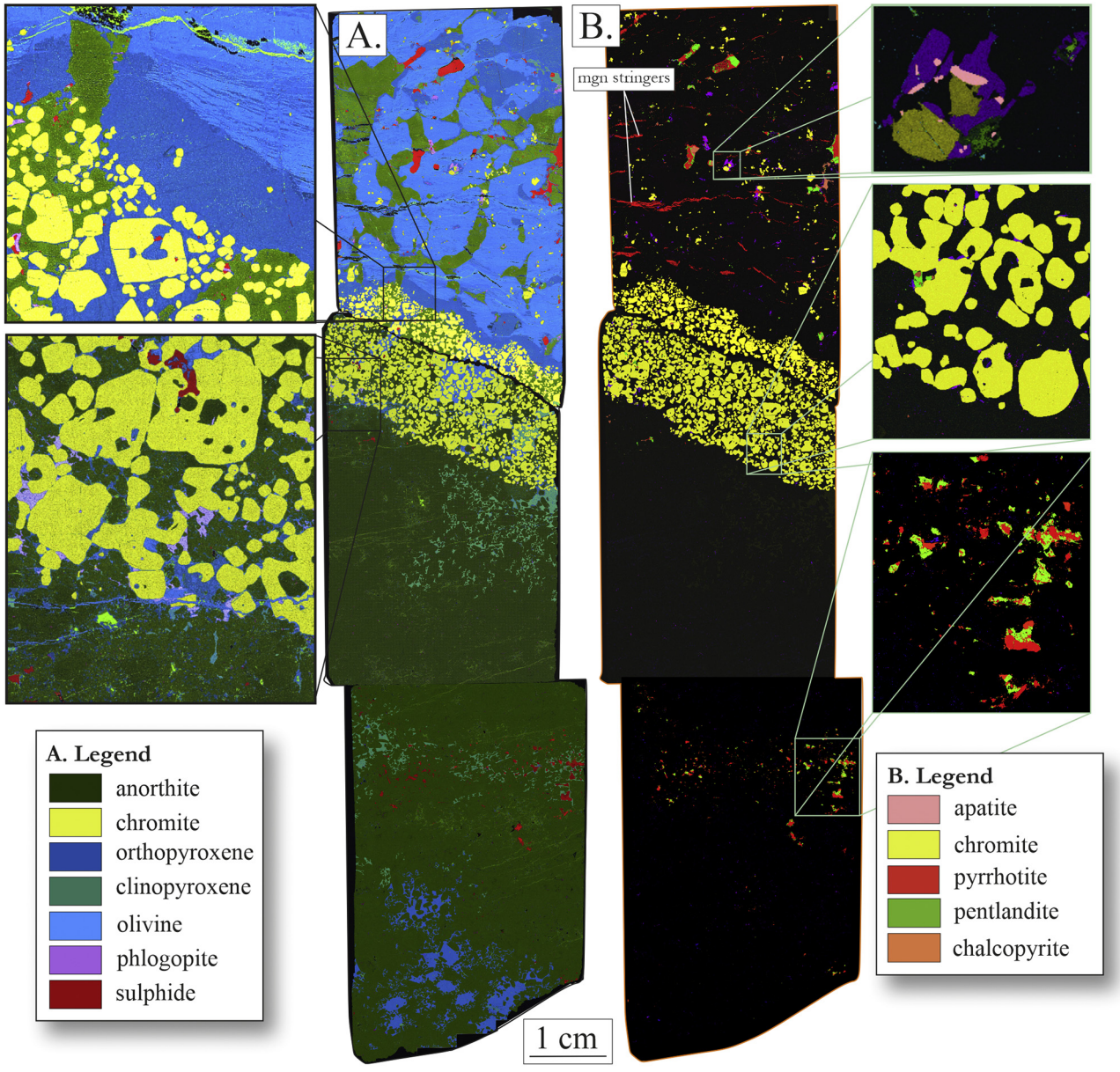

Fig. 5. (A) SEM-EDS map three polished thin sections of sample RPM-2 with enhanced areas of interest. The upper contact of the chromite seam is characterised by narrow undulations with fine, rounded chromite grains. The lower contact is sharp with more irregular chromite grains. (B) SEM-EDS accessory phase map. The upper right image is an apparent melt inclusion, comprising apatite, phlogopite, albite, and chromite.

pegmatoid (< 0.5%), both interstitially amongst the matrix and as inclusions within orthopyroxene. Interstitial phlogopite tends to be spatially associated with base metal sulphides and interstitial clinopyroxene. Phlogopite located within olivine is commonly associated with albite clinopyroxene, and apatite, somewhat analogous to the assemblage within melt inclusions described by Li et al. (2005). Base metal sulphides (~ 2.3%) show large variability in grain size (~ 2.2–3.1 mm) and consist dominantly of pyrrhotite and pentlandite, with lesser amounts of chalcopyrite. The sulphides mostly occur interstitial to orthopyroxene. Stringers of secondary magnetite extend sub-horizontally across the rock, sometimes coating base metal sulphides.

5.2. Merensky Reef at Impala mine

The specimen from Impala's Wildebeesfontein mine section was collected by B. Teigler and has been characterised by Hywel (2015). The specimen was cut and polished to expose the MR and mapped by SEM-EDS (Table 1; Fig. 6). The basal chromite stringer is approximately 13 cm-thick. Such thickened basal chromitites are described in footwall embayments at Impala and Rustenberg (*e.g.,* Ballhaus et al., 1988; Hutchinson et al., 2015; Latypov et al., 2017). Moreover, they are described on a regional scale, at the base of potholed reef across the WBC (Viljoen and Hieber, 1986; Viljoen, 1999). The bulk sample has PGE concentrations of 33.49 ppm Pt, 11.99 ppm Pd, 2.84 ppm Rh, 0.97 ppm Ir, 0.75 ppm Os, 5.4 ppm Ru and 0.35 ppm Au (unpublished data of authors, determined by Instrumental neutron activation analysis after Ni-sulphide fire assay at University of Quebec at Chicoutimi), *i.e.,* broadly similar to the element concentrations in thin Merensky chromite stringers (*e.g.*, Barnes and Maier, 2002), with the exception of Pd which has 5 times higher values in the present sample, resulting in much higher Pd/Ir and lower Pt/Pd values.

5.2.1. Footwall norite

The rock shows similar mineralogical and textural features as the footwall norite in the Rustenburg samples. The modal proportions of plagioclase, orthopyroxene and clinopyroxene are approximately 60:30:10. Orthopyroxene forms relatively large grains (~0.7–1.8 cm in diameter) that have massive internal domains surrounded by a branching network of orthopyroxene and clinopyroxene (~10%) that extends for ~5 mm into the interstitial space between surrounding subhedral plagioclase grains (0.5–2.6 cm in diameter). Although not quantitatively analysed, the rims of plagioclase grains appear to be more calcic than their cores. Base metal sulphides occur predominantly within plagioclase-rich domains of the norite and consist mainly of pyrrhotite and pentlandite, with lesser amounts of chalcopyrite. No chromite is observed in the rock. Trace amounts of phlogopite occur particularly within plagioclase-rich domains towards the top of the layer where it is spatially associated with base metal sulphides.

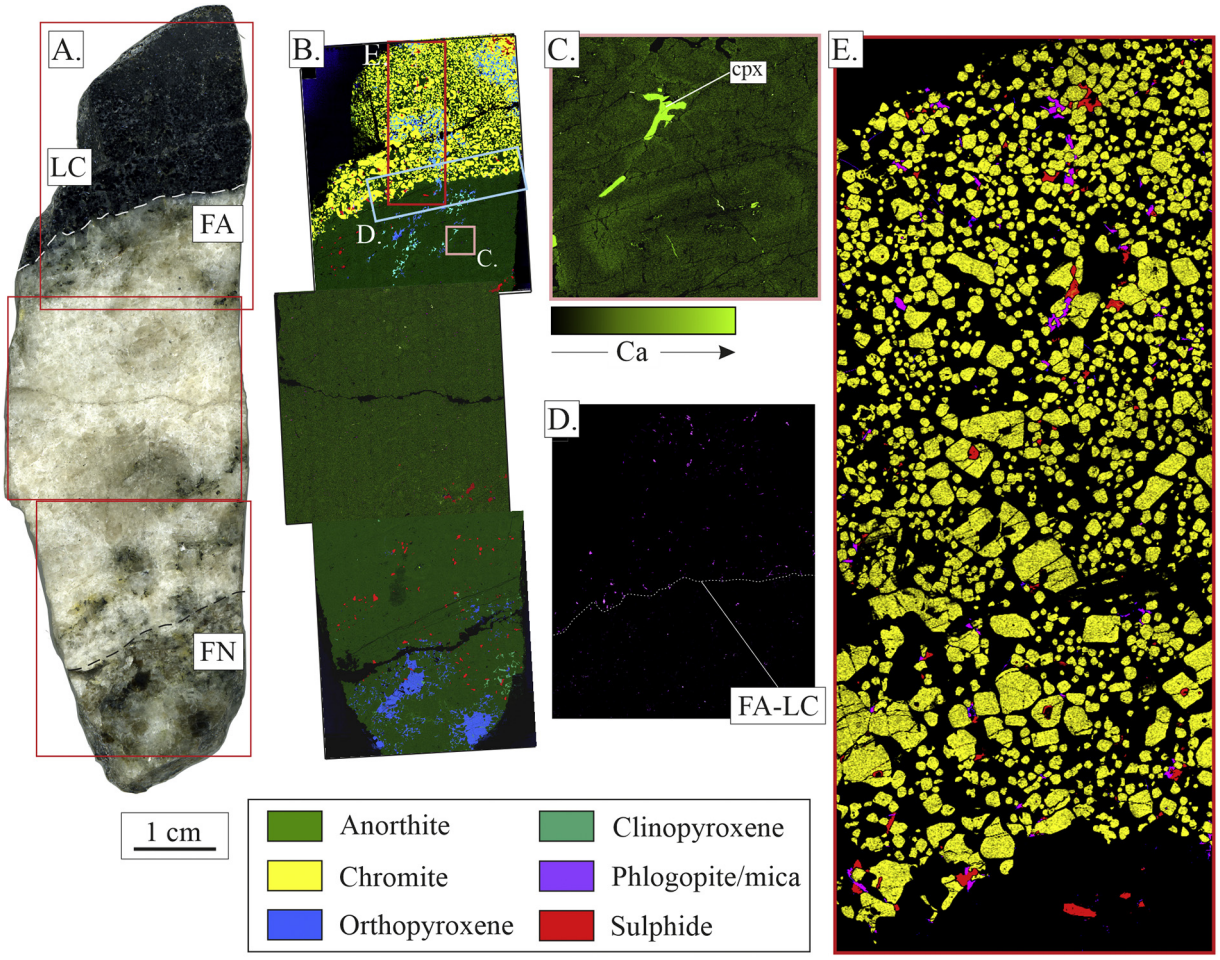

Fig. 6. (A) Photograph of sample IMP-BT, where LC = lower chromitite, FA = footwall anorthosite, FN = footwall norite. (B) SEM-EDS map of sample IMP-BT with enhanced areas of interest. (C) Reverse-zoned cumulus plagioclase in the FA. (D) Phlogopite occurrence along the lower contact of the LC. (E) Chromite-phlogopite-sulphide phase map of the LC. Note that sulphide and phlogopite are often in contact.

5.2.2. Footwall anorthosite

The layer has a similar thickness (~ 7–8 cm) as in sample RPM-1. The main component of the rock is subhedral plagioclase that shows relatively calcic rims. Along the base of the layer is a sub-horizontal, ~ 1-cm-thick horizon enriched in intercumulus clinopyroxene and base metal sulphides. Above this is a ~ 5 cm interval composed almost entirely of plagioclase, with only traces of interstitial clinopyroxene and phlogopite (each <0.5%). In the uppermost ~2 cm of the anorthosite there occur clusters of interstitial orthopyroxene and clinopyroxene which appear to be extensions of oikocrystic pyroxene in the overlying chromitite layer. Only few, small grains of phlogopite are present and no chromite is observed, but there are a few composite grains of base metal sulphides. The contact with the overlying chromite layer is sharp and fairly regular and shows an enhanced concentration of phlogopite, analogous to sample RPM-1.

5.2.3. Basal chromitite

Chromite grains have highly variable sizes and locally display vermiform and amoeboidal textures, particularly at the base of the layer. Intercumulus plagioclase is the primary oikocrystic phase (~ 29%) followed by orthopyroxene (~ 7.5%). Phlogopite occurs throughout the layer (~ 0.8%), located interstitial to chromite and plagioclase. Base metal sulphides constitute up to 10.3% of the interval. The grains (~ 1–7 mm in diameter) tend to be spatially associated with phlogopite. Notably, sulphides fill many of the inclusions in chromite. The sulphides are composed of equal proportions of pyrrhotite, pentlandite, and chalcopyrite.

5.3. Merensky Reef at the Karee mine

A halved drill-core specimen (~4 cm in diameter and ~16.8 cm in length) was collected from the Karee Mine. Six polished thin sections were cut from the specimen and mapped *via* SEM-EDS (Table 1; Fig. 7).

5.3.1. Footwall anorthosite

The rock forms the lowermost ~3–4 cm of the sample. Subhedral plagioclase (~ 94 modal %) is the main mineral constituent (~ 0.8–1.9 mm in diameter) and shows no obvious compositional zoning (~ An_{75}–An_{80}). Other phases include clinopyroxene (~ 1.8 modal %, < 1.8 mm in diameter) which becomes more prevalent towards the top of the layer, and orthopyroxene (~ 1.1 modal %, < 0.6 mm in diameter). Very fine-grained sulphides occur as patchy disseminations (0.6–1 mm) that tend to form diffuse sub-horizontal layers. No chromite or phlogopite is observed.

5.3.2. Lower chromitite

The layer measures ~1 cm in thickness and has sharp and straight upper and lower contacts. The size of the chromite grains varies non-systematically across the layer, but grains displaying vermiform and amoeboidal textures appear to be more common near the base. Larger grains (~ 1.5–2 mm) tend to be annealed and often contain rounded inclusions of matrix material. Plagioclase forms large oikocrysts which occupy the interstitial space in the lower ~75% of the chromitite layer. The anorthite content of plagioclase broadly overlaps with that in the footwall anorthosite, except for the upper portion of the chromite stringer where An content of plagioclase is slightly lower (~ An_{60}). Oikocrystic orthopyroxene mainly occurs in the upper ~25% of the layer. Base metal sulphides (~ 1.7%) tend to be much smaller than in the footwall or hanging wall layers.

5.3.3. Pyroxenite

This forms the remaining ~8–9 cm of the sample and consists predominantly of anhedral orthopyroxene (~ 83 modal %, < 0.5 cm in diameter), with interstitial plagioclase (~ 4.6%), interstitial clinopyroxene (~ 5.2%), base metal sulphides (~ 3.5%), anhedral chromite (< 1%) and phlogopite (~ 1.3%) constituting the remainder of the rock. Interstitial plagioclase displaying highly variable anorthite content (~ An_{30}–An_{80}) forms a discontinuous network through this interval. Clinopyroxene often occurs in direct contact with interstitial phlogopite. A large (~ 1.7 cm) subhedral clinopyroxene oikocryst occurs at the top of the sample, which hosts numerous inclusions of orthopyroxene. Phlogopite becomes more abundant and coarser-grained with height. Coarse-grained, interstitial base metal sulphides occur predominantly in plagioclase-poor domains of the pyroxenite. They consist of approximately even proportions of pyrrhotite, pentlandite, and chalcopyrite.

In situ Sr isotopes were determined on fifty-nine spots at seven stratigraphic levels (two in the anorthosite and five in the pyroxenite; Fig. 7). The data show a subtle increase in Sr_i with height. The two analysed horizons in the anorthosite have average Sr_i values of 0.70627 ± 0.00008 and 0.70637 ± 0.00008 (2σ), whereas the five horizons analysed in the pyroxenite show an average Sr_i range of 0.70640 ± 0.00007 to 0.70655 ± 0.00008. The sample just below the chromitite stringer shows the lowest average Sr_i (0.70627 ± 0.0008) and greatest variation in Sr_i (0.70582–0.70655), whereas the sample in the centre of the pyroxenite shows the highest average Sr_i (0.70642 ± 0.00007).

5.4. Merensky Reef at the Northam Platinum Mine

The analysed MR at Northam Mine consists of so-called NP2 Reef that resembles the non-pegmatoidal contact facies displayed at Rustenberg, Impala, and Karee. At Northam, this constitutes the regional pothole reef, in which the MCU is underlain by anorthosite and troctolite.

5.4.1. Sample NTH48c

The sample represents the non-pegmatoidal MR and its immediate anorthosite-norite footwall. The footwall contains a ~ 5-cm-thick pyroxenite band, which represents one of several pyroxenite stringers observed in the MR FW (Table 1; Fig. 8). The sample was mapped using the Maia Mapper μXRF.

5.4.1.1. Footwall norite-anorthosite and pyroxenite-norite layer. At the base of the sample is norite comprising fine- to medium-grained anhedral orthopyroxene (~ 26%) elongated sub-parallel to the layering and showing extensive intercumulus overgrowth within a matrix of subhedral plagioclase. Traces of clinopyroxene and phlogopite are also present, but there are only very fine grains of base metal sulphides (predominantly chalcopyrite), and no chromite. The norite shows a somewhat diffuse, but locally sharp contact to a ~ 2–4 cm wide composite melanorite-pyroxenite layer, consisting of a ~ 1–2 cm basal melanorite, a ~ 1–2 cm central pyroxenite and a ~ 1–2 cm upper leuconorite. The central orthopyroxenite is of particular interest: it consists of mostly subhedral orthopyroxene (~ 54%) in a matrix of interstitial plagioclase (~ 19%) and less abundant clinopyroxene (~ 3.7%). A large anhedral grain of clinopyroxene (~ 1.4 cm in diameter) hosting several orthopyroxene inclusions appears to push apart the surrounding orthopyroxenes causing a subtle widening of the layer. A few grains of chromite and fine-grained phlogopite occur throughout the orthopyroxenite, and there are numerous base metal sulphides (~ 9%), occurring interstitial to orthopyroxene. The sulphide assemblage is dominated by pyrrhotite rimmed by pentlandite, and spatially removed chalcopyrite. The size and volume of base metal sulphides decrease towards the margin of the pyroxenite layer. Rare PGM are located peripheral to the sulphide minerals.

The anorthosite above the composite pyroxenite-norite layer forms a thin (~ 0.5–1 cm) adcumulate layer containing minor (< 5%) poikilitic clinopyroxene. No other minerals are observed. The subhedral plagioclase grains are not visibly zoned. The contact to the overlying chromitite is knife-sharp and gently undulating, whereas the contact to the footwall norite is somewhat more diffuse.

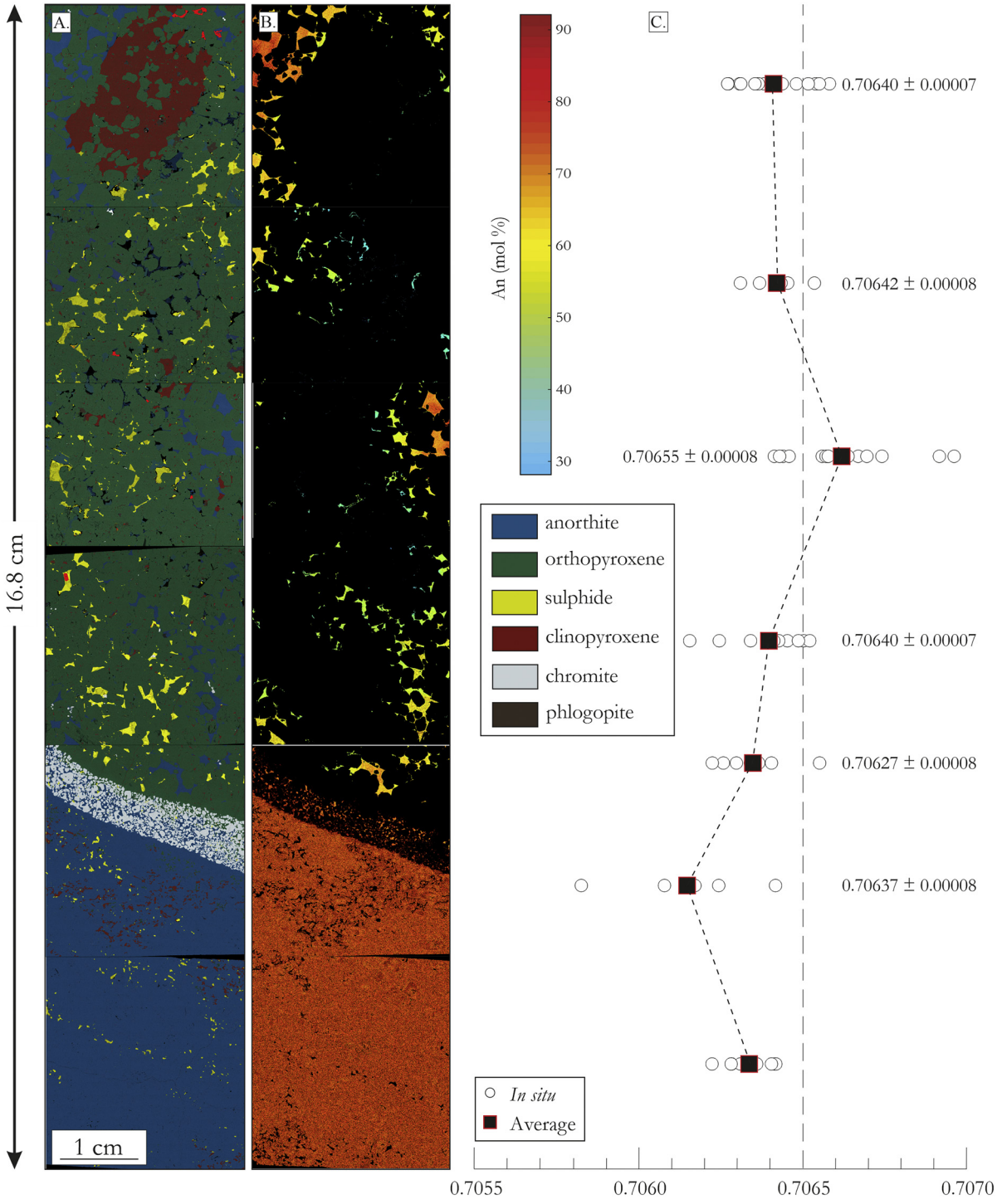

Fig. 7. (A) SEM-EDS map of sample KR-1. (B) An map of sample KR-1, note that the cores of plagioclase oikocrysts generally possess higher An content than the exteriors. (C) *In situ* Sr isotope composition of plagioclase throughout the sample.

5.4.1.2. Merensky lower chromitite. The base of the chromitite stringer is composed of very fine-grained chromite grains in a matrix of intercumulus clinopyroxene and less abundant plagioclase. The basal interval is overlain by relatively more heterogenous and coarser-grained chromitite consisting of domains of densely packed chromite as well as domains in which disseminated chromite (< 0.8 cm), commonly showing highly amoeboidal, atoll-like and annealed textures, is set in a matrix of plagioclase (~ 35%) and large (up to 3 cm) orthopyroxene oikocrysts (~ 7%). Clinopyroxene tends to be intergrown with plagioclase and forms rare oikocrysts enclosing rounded orthopyroxene inclusions. Phlogopite (< 0.5%) occurs throughout the layer and tends to be spatially associated with base metal sulphides (~ 7.5%). The latter have markedly smaller grain sizes than sulphides in the footwall pyroxenite layer. They are disseminated throughout the layer, comprising broadly even proportions of pyrrhotite, pentlandite, and chalcopyrite. Sulphides are particularly concentrated in chromite-rich domains where they predominantly occur interstitial to chromite. Several PGM are observed, occurring at or near the margins of base metal sulphides.

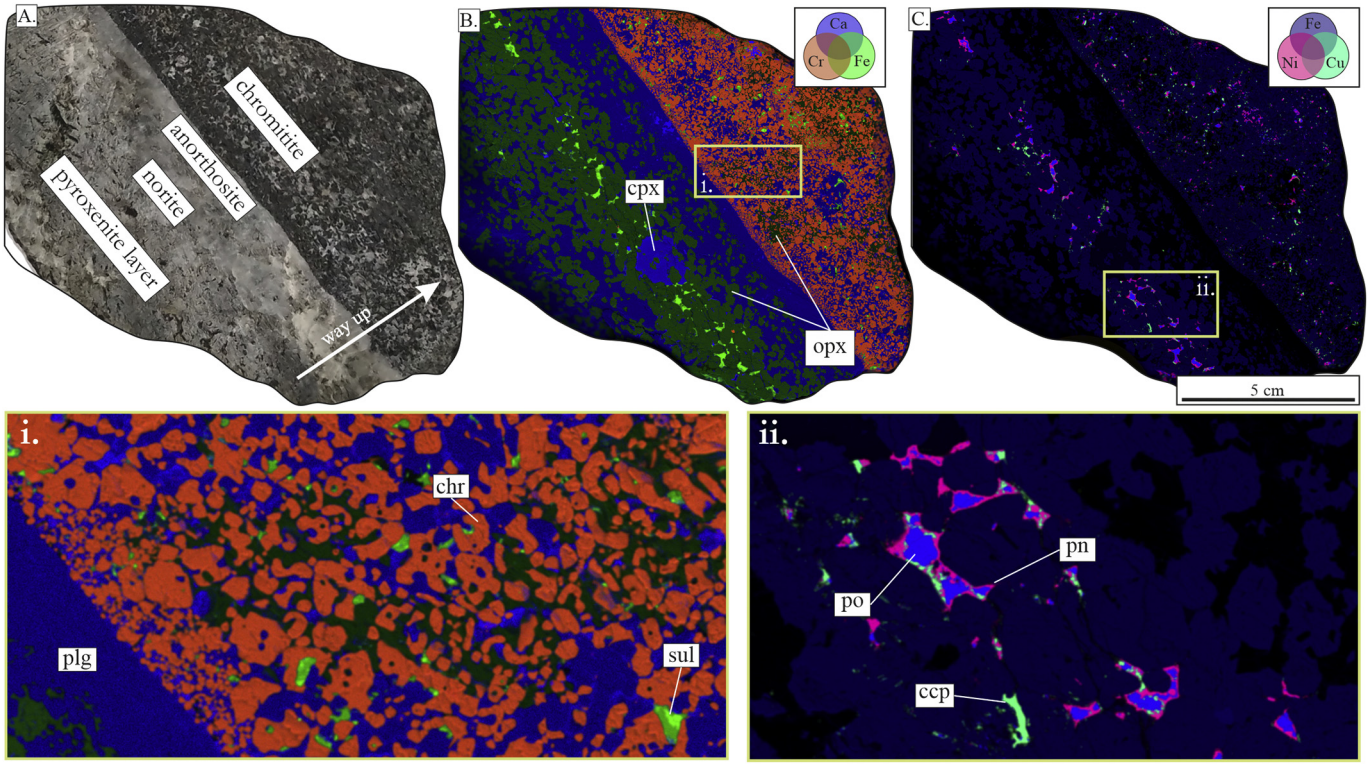

Fig. 8. (A) Photograph of sample NTH-48c. (B) μXRF Cr-Ca-Fe element map with an enhanced area of interest. Observe the knife-sharp contact between the chromitite and anorthosite, as well as the change in chromite grain size. (C) μXRF Fe-Ni-Cu element map with an enhanced area of interest. Note the concentration of base metal sulphides in the central norite layer. Pentlandite lines the exteriors of interstitial pyrrhotite.

5.4.2. Sample NTH-10b

Sample NTH-10b is an olivine norite in the footwall of non-pegmatoidal NP2 reef intersected in drill core BH-10-4930. These rocks have previously been termed troctolites by Roberts et al. (2007), but in our sample the proportion of orthopyroxene is >10%. This sample was mapped by SEM-EDS (Table 1; Fig. 9).

The sample is composed of olivine (~ 8.8%), plagioclase (~ 67%), orthopyroxene (~ 18%), and base metal sulphides (~ 2.7%), with traces of clinopyroxene (~ 2.2%), phlogopite (~ 0.9%), apatite (< 0.1%), and zircon (< 0.1%). The olivine is anhedral and medium grained (~ 1.3–4.2 mm in diameter). It is mantled by orthopyroxene which forms finger-like extensions into the surrounding intercumulus space. Plagioclase forms several mm-wide, pod-like anorthosite adcumulate domains within a network of orthocumulate troctolite. Although not quantitatively analysed, the plagioclase grains appear to display reverse compositional zoning, from ~ An_{75-80} in the core to An_{84-88} in the rim. Clinopyroxene may form anhedral grains between plagioclase. Chromite is rare, forming a few small grains associated with orthopyroxene. Phlogopite tends to be spatially associated with base metal sulphides, both occurring within orthopyroxene overgrowths of olivine and nearby plagioclase but being rare in plagioclase rich domains and entirely absent within olivine. The sulphides are typically disseminated forming relatively coarse (~ 0.3 to 0.7 mm in diameter) composite grains consisting mainly of pyrrhotite and pentlandite, whereas chalcopyrite is typically found in the surrounding matrix.

In one olivine grain an irregular inclusion (~ 0.96 mm × 0.51 mm; interpreted to be a melt inclusion) containing Fe-rich orthopyroxene (~ 42%), sodic plagioclase (~ 28%), phlogopite (~ 24%), apatite, and zircon was identified. The composition of apatite was determined by SED-EDS to have up to ~2.5 wt.% Cl and ~ 1.3 wt.% ∑REE.

5.4.3. Sample NTH047

Sample NTH47–110 represents the footwall olivine norite and anorthosite of the NP2 reef. It was mapped by the Maia Mapper μXRF (Table 1; Fig. 10).

5.4.3.1. Footwall olivine norite. The sample displays similar olivine-orthopyroxene textures to NTH-10b, in that anhedral olivine (~ 3.4%) is surrounded by anhedral orthopyroxene (< 0.8 cm in length, with a mode of ~20.3%) forming patchy, intercumulus domains, typically associated with accessory intercumulus clinopyroxene. Centimetre-scale domains of almost pure plagioclase occur between the orthopyroxene grains. No chromite or phlogopite are observed. Base metal sulphides are disseminated throughout much of the rock, with the exception of the anorthositic domains and a several-cm-wide noritic portion near the base of the sample that shows relatively Fe-rich orthopyroxene cores. PGM occur near the margins of base metal sulphides. The rock displays an irregular contact with the overlying footwall anorthosite.

5.4.3.2. Footwall anorthosite. The interval is ~4–5 cm in width and is compartmentalised into plagioclase-rich and clinopyroxene-rich domains. No chromite or phlogopite are observed in this interval. Plagioclase-rich domains contain only traces of intercumulus clinopyroxene and base metal sulphides. Clinopyroxene-rich domains contain traces of intercumulus Fe-poor orthopyroxenes. Base metal sulphides (po ~ 32.2%, pn ~ 57.1%, and ccp ~ 10.8%) are spatially associated with the clinopyroxene-rich domains. Discrete PGM are present mostly near the margins of base metal sulphides.

5.4.4. Sample NTH-04612

Sample NTH-4612 covers the interval from footwall olivine norite into the non-pegmatoidal MR of the NP2 reef and was imaged by the

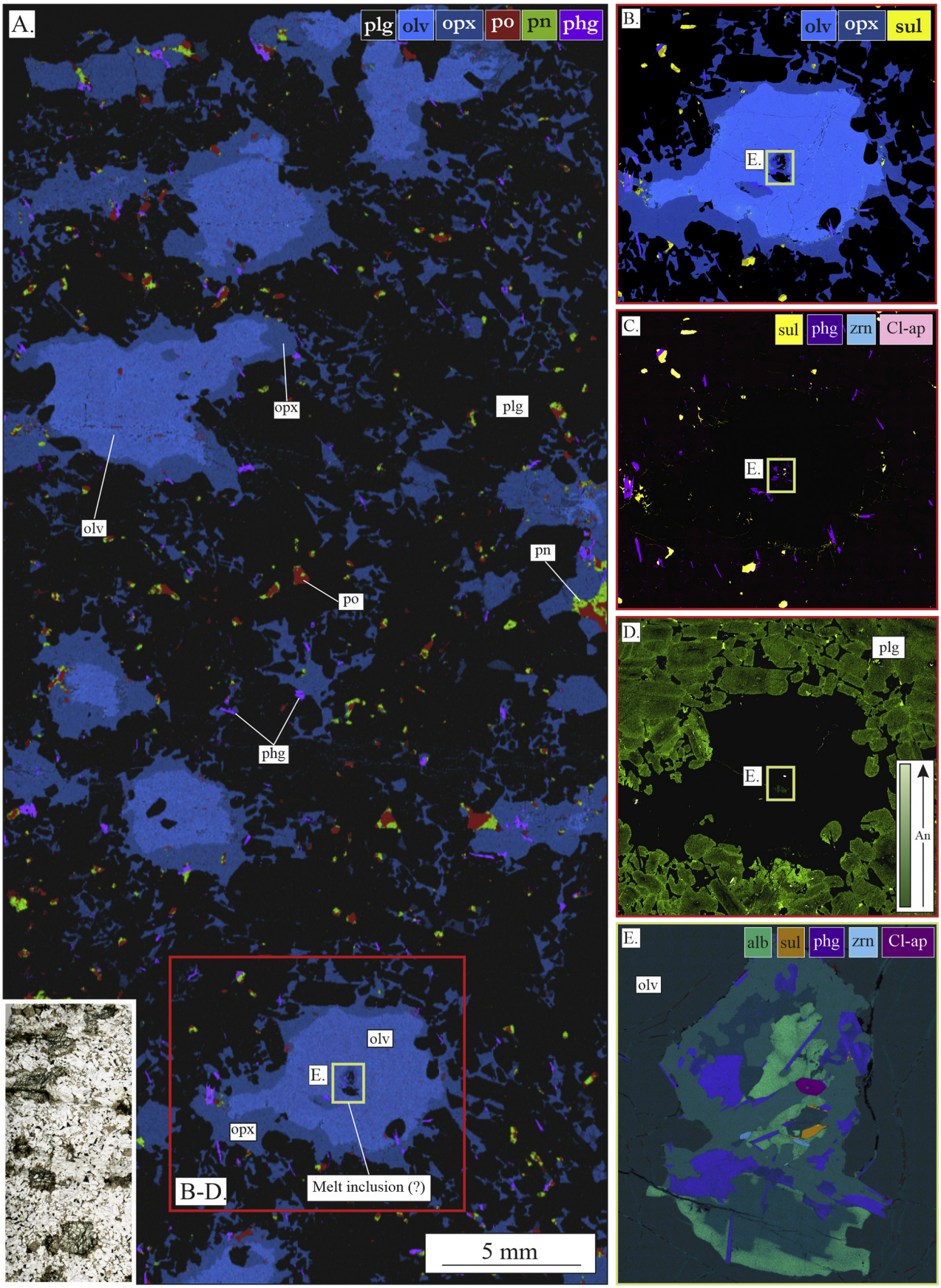

Fig. 9. (A) SEM-EDS map of sample NTH-10b. (B–D) Enhanced image of an olivine-orthopyroxene oikocryst, which shows the occurrence of sulphide and phlogopite around the olivine (olv) grain and reverse oscillatory zoning in surrounding cumulus plagioclase. (E) Enhanced element map of a suspected melt inclusion, which comprises chloroapatite (Cl-ap), phlogopite (phg), albite (alb), sulphide, and zircon (zrn).

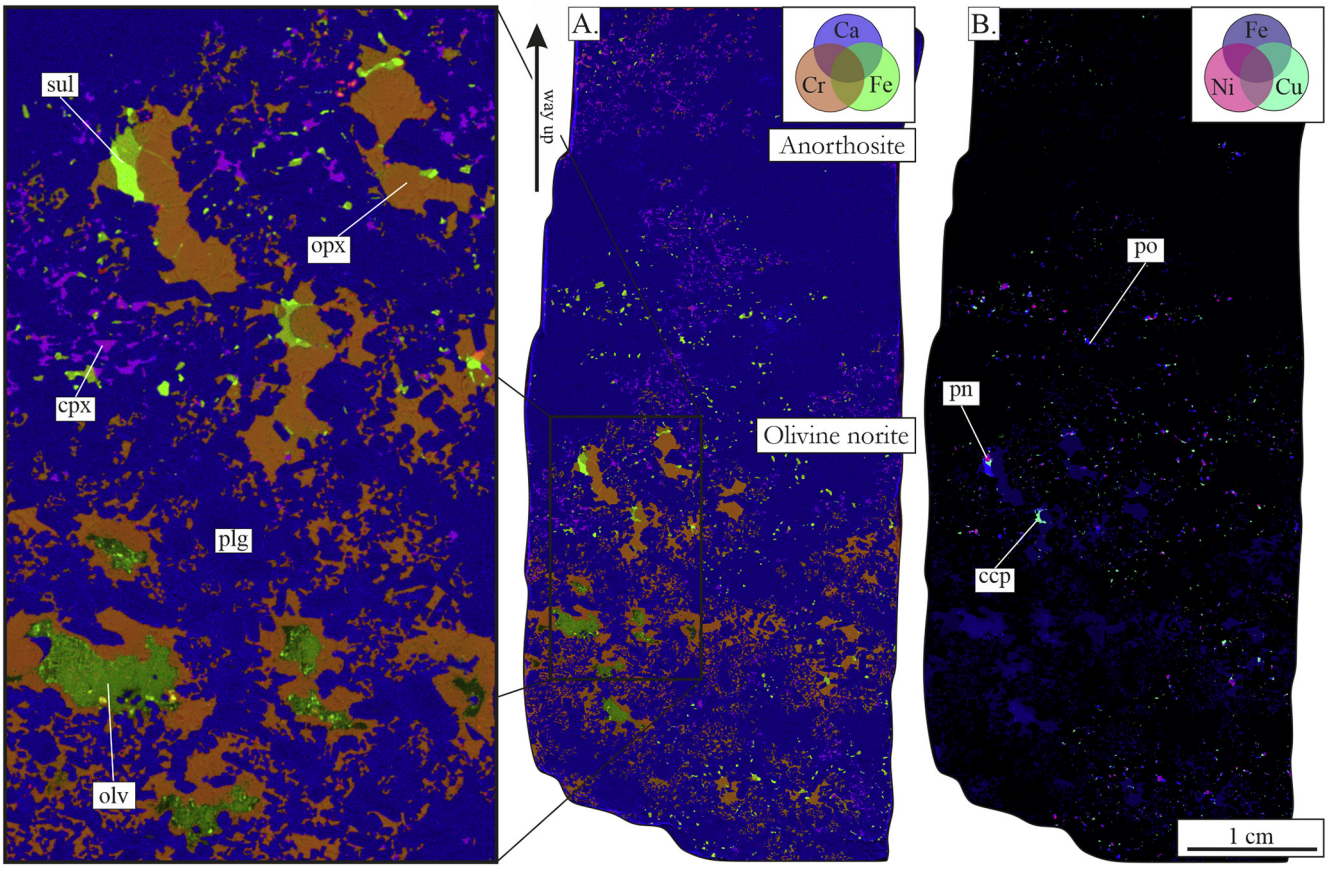

Fig. 10. (a) μXRF Ca-Cr-Fe element map of sample NTH047, with an enhanced area of interest highlighting olivine-orthopyroxene mantling. (b) μXRF Fe-Ni-Cu element map showing the distribution of base metal sulphide.

Maia Mapper μXRF. In this sample, the footwall olivine norite shares a sharp contact with a diffuse silicate-bearing chromite seam, in which chromite is primarily concentrated in stringers or pods (Table 1; Fig. 11).

5.4.4.1. Footwall olivine norite. The footwall to the MR consists of olivine norite. The bulk of the rock consists of subhedral plagioclase (2–4.5 mm in diameter, 61.2 modal %) showing reverse compositional zonation. Olivine constitutes ~12% of the rock and forms anhedral grains (3–5 mm in diameter) or grain aggregates that tend to be elongated sub-parallel to the layering (up to 8 mm in diameter). Many olivine grains contain relatively small, rounded inclusions of plagioclase and most are mantled by orthopyroxene, particularly along the upper side of the grains. Base metal sulphides (~ 1.2%) and phlogopite (~ 1%) are preferentially located interstitial to plagioclase, or within orthopyroxene, but they are absent from olivine. The sulphides form fine disseminations of composite pyrrhotite-pentlandite grains, whereas chalcopyrite mostly forms distinct grains. Phlogopite tends to be associated with sulphide and commonly forms elongate laths that display the same orientation in cm-scale domains, which is roughly parallel with the overlying diffuse chromite seam. Chromite forms rare (~ 0.7%) anhedral grains of variable size (0.5–2.5 mm in diameter), mainly associated with plagioclase or orthopyroxene. Only traces of interstitial clinopyroxene are present. Rare PGM occur near the margins of base metal sulphides.

5.4.4.2. Merensky pyroxenite and chromite pods. The contact between the Merensky pyroxenite and the footwall olivine norite is relatively straight, but somewhat diffuse. Some segments of the contact are enriched in anhedral, amoeboidal, and sometimes atoll-like chromite, but elsewhere chromite is absent, and medium- to coarse-grained orthopyroxenite orthocumulate directly overlies the footwall olivine norite. The Merensky pyroxenite in this sample has very heterogenous modal proportions; The main minerals are medium-grained cumulus orthopyroxene (~ 64%) which tends to be relatively Cr-poor when in direct contact with chromite grains. Interstitial plagioclase constitutes ~26% and chromite ~10% of the rock. Patchy domains that are highly enriched in chromite may form massive chromitite pods, but elsewhere the pyroxenite is relatively devoid of chromite. The chromite-rich domains are characterised by coarse-grained, commonly annealed chromite grains embedded in an interstitial matrix of base metal sulphides, *i.e.,* there is a strong spatial association of chromite and sulphide. Chalcopyrite, pyrrhotite and pentlandite occur in broadly even proportions. In the chromite-poor domains, chromite grains are typically found within intercumulus plagioclase or along the margin of orthopyroxene, whereas few chromite grains are included in orthopyroxene. The rock contains little clinopyroxene or phlogopite, but many discrete titanite grains are observed at the boundaries of chromite grains.

6. Discussion

6.1. Footwall norite

The petrographic characteristics of the footwall norite (Figs. 2, 5 and 6) are typical of MR footwall norite across the WBC (Maier and Eales, 1997). The unit shows subtle layering and consists of anhedral, poikilitic orthopyroxene with rounded plagioclase inclusions and narrow intercumulus orthopyroxene and clinopyroxene haloes in a matrix of predominantly concentrically-zoned, subhedral plagioclase. The proportions of orthopyroxene to plagioclase are broadly cotectic (40:60)

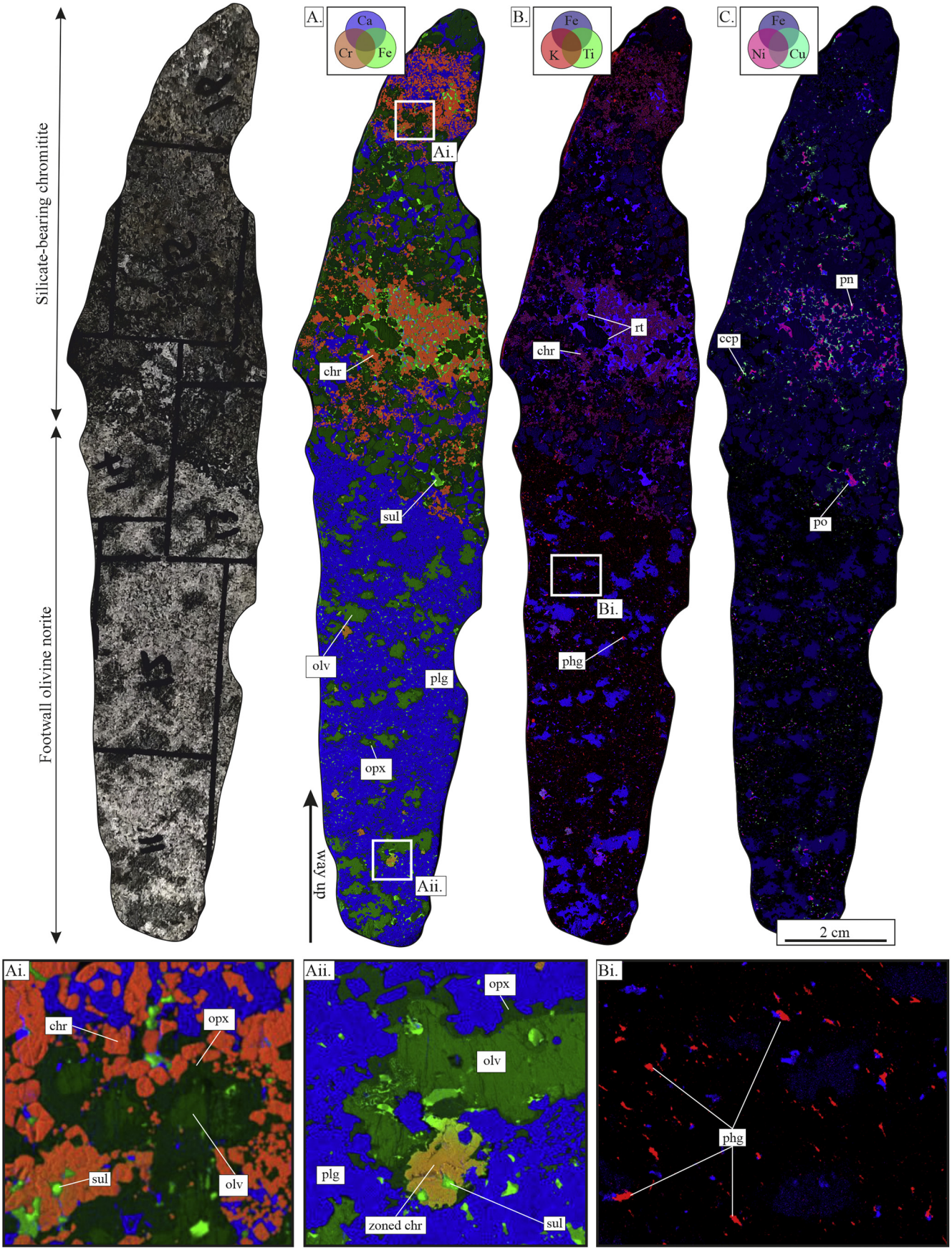

Fig. 11. (A) μXRF Ca-Cr-Fe element map of sample NTH-4612 with enhanced areas of interest, showing (Ai) olivine-orthopyroxene mantling in the silicate-bearing chromitite when in contact with chromite and (Aii) compositional zoning of chromite in the footwall when in contact with orthopyroxene. (B) μXRF Fe-K-Ti element map with an enhanced area of interest showing the abundance and orientation of phlogopite in the footwall. (C) μXRF Fe-Ni-Cu element map showing the distribution of base metal sulphides.

and there are only traces (« 1%) of very fine-grained chromite, phlogopite, and base metal sulphides, which mostly occur near to the contact with the anorthosite. Where present, sulphides consistently occur with interstitial clinopyroxene. There are no resolvable PGMs in the footwall norite. Whole-rock compositional data of Maier and Eales (1997) show broadly similar $Mg\#_{opx}$ as in UCZ pyroxenites (~ 75–80), decoupling of $Mg\#_{opx}$ from An_{plg}, and relatively low incompatible trace element concentrations (typically <10 ppm Zr). Maier and Eales (1997) interpreted these data to reflect gravitative crystal sorting and efficient compaction (< 10% trapped intercumulus liquid; see also Wilson et al., 1999).

6.2. Footwall anorthosite

The footwall anorthosite (Figs. 2, 5 and 6) consists almost exclusively of subhedral plagioclase with small proportions of interstitial clinopyroxene mostly in the upper third of the interval or at the base of potholes. Interpreting the origin of anorthosite layers remains a major petrological challenge and it is unlikely that all Bushveld anorthosites formed in the same manner. Traces of orthopyroxene, phlogopite, and chromite occur in the upper third of the unit. Finely disseminated sulphides typically form sub-vertical channels and sub-horizontal layers (*cf.*, Barnes and Maier, 2002; Godel et al., 2006). The latter are concentrated along the irregular contact with the underlying norite suggesting that the contact constituted a permeability barrier.

Interpreting the origin of anorthosite layers remains a major petrological challenge. Proposed models included crystal flotation (Vermaak, 1976; Raedeke and McCallum, 1984), partial melting of mafic phases in protogabbronorite producing an anorthositic restite (Eales et al., 1986; Boudreau, 1988; McBirney and Sonnenthal, 1990; Nicholson and Mathez, 1991; Sonnenthal, 1992), metasomatism or sub-solidus reaction driven by chemical gradients (Mathez and Mey, 2005; Mathez and Kinzler, 2017), phase separation during granular flow (Maier et al., 2013), gravitational draining of residual Fe-rich melt (Scoates et al., 2010; Maier et al., 2016) and precipitation from magmas supersaturated in plagioclase (Latypov et al., 2020).

The partial melting model implies that the rock temporarily consisted of relatively permeable mush, consistent with the downward percolation of Merensky Reef sulphides, the variable An content of plagioclase (up to An_{85}; Naldrett et al., 1986), and the reversed zonation (this study; Hunt et al., 2018). However, Barnes and Maier (2002) argued that the presence of a sub-horizontal lamination is more consistent with a primary igneous texture. Furthermore, Holness et al. (2017) argued that mush zones in the Bushveld Complex cannot have exceeded ~4 m, consistent with observations of this study.

Many anorthosites of the UCZ contain >10 vol% of pyroxene oikocrysts and subordinate olivine (*e.g.,* Maier, 1995), which gave rise to the term 'mottled anorthosite' widely used in the Bushveld literature. Other than in the immediate MR footwall, near-monomineralic anorthosites are confined to coronas below and around ultramafic rocks, *e.g.,* the 'boulders' of the Boulder Bed (Jones, 1976), around ultramafic bodies in the Flatreef, (Grobler et al., 2019) and bracketing some chromitites. Some of these anorthosites contain elevated PGE (Maier and Barnes, 2003, 2008) and likely formed in the same way as the MR anorthosite.

6.3. Footwall olivine norite

Footwall olivine norite (Figs. 9–11) commonly underlies the MR in regional potholes facies at Northam mine (Roberts et al., 2007), and may occur locally elsewhere, *e.g.,* in the southwestern Bushveld at Wolhuterskop (unpublished data of Maier). This unit is characterised by resorbed, anhedral olivine containing rounded plagioclase inclusions, orthopyroxene reaction rims, and intercumulus orthopyroxene and clinopyroxene halos in a matrix of subhedral plagioclase. Observations of particular interest include: (i) reverse-zoned plagioclase with locally well-defined triple junctions (Fig. 9), (ii) a high abundance of accessory phlogopite, commonly occurring at the outer edge of orthopyroxene reaction rims around olivine (Figs. 9 and 11), (iii) orthopyroxene overgrowths are generally thicker along the upper margin of olivine grains (Fig. 11), (iv) sulphides are rarely present within olivine, but commonly occur at the outer edges of orthopyroxene (with phlogopite) and interstitial to matrix plagioclase, and (v) the occurrence of polymineralic inclusions in olivine (interpreted as melt inclusions), comprising sodic plagioclase, phlogopite, Cl-apatite, zircon, and sulphide.

Roberts et al. (2007) proposed that the unit formed in response to the downward percolation of sulphide-bearing, high-MgO basaltic magma from the MR into partially molten anorthosite. Pre-existing pyroxene and albitic rims of plagioclase would have been consumed by the relatively unevolved melt, which went on to crystallise olivine and peritectic orthopyroxene. However, in this model, we would possibly expect to see sulphide inclusions in the olivine, rather than forming channel ways around it (Fig. 10). It is also difficult to reconcile the observed heterogeneous distribution of chromite with this model. An alternative explanation is that the olivine norite formed in response to hydration melting of a pre-existing norite, which stabilised olivine and facilitated the downward percolation of sulphide liquid (Boudreau, 1999). A hydromagmatic origin may be supported by the presence of the melt inclusions, Cl-apatite, and high relative proportions of phlogopite observed in this study, but the absence of clear fluid migration pathways characterised by elevated quartz and mica contents, compositional changes in plagioclase, and the presence of pargasitic hornblende is problematic (*cf.,* Roberts et al., 2007).

6.4. Footwall pyroxenite-norite layer

The footwall pyroxenite-norite-anorthosite layer at Northam (Fig. 8) closely resembles apophyses that undercut the MR described by Latypov et al., 2017, which comprises a sulphide-rich pyroxenite core zone and sulphide-poor leuconorite-anorthosite rims. Key observations from Fig. 8 include: (i) orthopyroxene in the pyroxenite is significantly coarser grained than orthopyroxene in the leuconorite, (ii) sulphides (and a few chromite grains) are concentrated in the central pyroxenitic portion of the layer, but absent from the marginal leuconorite-anorthosite, (iii) the leuconorite-anorthosite contact is irregular and knife-sharp, and (v) there is very little mica, quartz, or amphibole.

The concentration of the largest and densest phases (accessory chromite, orthopyroxene and sulphide) towards the centre of the layer is consistent with grain-dispersive pressure or the Magnus effect operating in flowing crystal slurries (Komar, 1972). However, crystal slurries cannot flow when exceeding a critical crystal content (~ 55%; Marsh, 2013). The lack of clinopyroxene, phlogopite, and quartz suggests that there was insufficient residual liquid to support granular flow, unless the residual liquid was effectively expelled/drained. Sulphide concentrated in the centre of the apophyse exceeds its cotectic proportion which is difficult to reconcile with *in situ* crystallisation.

6.5. Merensky chromitite layers

The chromitite stringers studied here are representative of the various types of the MR exposed in the WBC; in some intersections the reef shows two chromitite stringers bracketing the pegmatoid (RPM and Karee), other intersections have just one chromitite at the base of the MR (Impala and Northam), and one of our samples from Northam lacks a continuous chromite stringer but instead contains irregular chromite pods within the Merensky pyroxenite (NTH-04612). The anorthosite-chromite contact is typically knife-sharp, irregular and characterised by skeletal to amoeboidal chromite, whereas the chromitite-pegmatoid-chromite contacts are irregular, diffuse, and characterised by fine-grained, equant chromite (Figs. 2, 5, 6, 7, and Supplementary Fig. 1). Some samples show sub-vertical chains of chromite (Fig. 2). Accessory sulphide and phlogopite are generally spatially

associated and heterogeneously distributed throughout the chromitite stringers, and the upper stringer may be enriched in rutile (Supplementary Fig. 2). The chromitites contain the greatest concentration of PGM amongst the reef lithologies (Fig. 3).

Similar chromite textures as the ones described here have been documented in several previous studies. Eales and Reynolds (1986) interpret cuspate/lobate grains to be a result of annealing of originally finer disseminated grains. Furthermore, they propose chromite chains to form by *in situ* nucleation at growth at the base of a fresh magma. Vukmanovic et al. (2013) detailed amoeboidal and skeletal chromite with rounded silicate inclusions in the lower chromite and fine, idiomorphic chromite in the upper chromitite. They proposed that irregular chromite grains in the lower chromite formed in response to supercooling, whereas the upper chromitite crystallised under equilibrated temperatures. In addition, Vukmanovic et al. (2013) propose large amoeboidal grains form as a result of compaction and not sintering, since the observed formation microstructures are inconsistent with sintering. Hutchinson et al. (2015) studied chromitites at RPM and Impala that comprise one chromitite at the base of the non-pegmatoidal reef. They describe amoeboidal chromite at the base and fine, equant chromite in the upper portion. The authors argued that the two chromitites crystallised from two successive magma influxes, the first containing entrained, irregular chromite that became overlain by pyroxenite. The pyroxenite was then eroded by a second magma influx from which the upper chromite seam precipitated in response to magma mixing. To explain the amoeboidal grains the authors proposed a model of chemical corrosion by fluids.

Our data are consistent with many of the previous observations and interpretations, notably the evidence for *in situ* growth. However, the trigger for chromite nucleation is less clear. Vukmanovic et al. (2013) argued for mixing between replenishing melt and a partial melt of the floor rocks. However, if the floor was in a partially molten state when the chromitite formed, one would expect that some chromite grains would have sunk into the mush, unless the grains were too large or grains clustered. Li et al. (2005) documented evolved, hydrous melt inclusions in chromite, which infers the presence of a hydrous silicate melt at the time of their formation (*cf.*, Boudreau, 1991; Nicholson and Mathez, 1991). Such features have also been documented in the pegmatoid in this study. However, such models are seemingly inconsistent with the paucity of intercumulus hydrous phases. In comparison, cumulates formed from hydrous magmas in some other layered intrusions, *e.g.,* Windimurra (Ivanic et al., 2015) and Nova (Maier et al., 2016) tend to be enriched in hydrous phases.

We have considered whether the supercooling textures of the chromitite could have formed due to rapid H_2O loss as a result of CO_2 influx (see Kokh et al., 2017; Caricchi et al., 2018). Carbon dioxide could have been derived from dehydration of the Transvaal dolomitic platform which underlies the Bushveld Complex and has locally been assimilated and reduced to calc-silicate (*e.g.,* Wallmach et al., 1995; Grobler et al., 2019). The presence of CO_2-rich supercritical fluids is supported by the presence of magmatic graphite in the UCZ (Mathez et al., 1989) and CO_2-rich fluid inclusions (Buthelezi, 2018). However, no carbonate or graphite was documented in this study and it remains unclear why such a process would only have affected the basal Merensky chromitite, but no other layer in the Critical Zone.

Lastly, there is some evidence for hydrodynamic processes, *e.g.,* in the form of the thickened chromite seams that are preferentially found in footwall troughs (Maier et al., 2013; Forien et al., 2015). The presence of irregular chromite pods (*e.g.,* Fig. 11) may also be explained by mechanical sorting models.

Another aspect of the chromitite stringers that remains poorly understood is their enrichment in PGE, at relatively low sulphide content. Barnes and Maier (2002) found ~50 ppm PGE in the seams. Sulphides are spatially particularly closely associated with chromite in Northam sample NTH-04612. Godel et al. (2006) argued that the chromite seams acted as permeability barriers to downward percolating sulphide melt, but in all our maps chromitite layers are clearly orthocumulates inconsistent with low permeability.

Possibly, sulphides were partially resorbed by late stage fluids (Li et al., 2005) or by reaction of sulphide with chromite (Naldrett and Lehmann, 1988). These processes could possibly have contributed to the concentration of PGM along the margins of sulphides (see Supplementary Fig. 1).

6.6. Merensky pegmatoid

The MR pegmatoid is unusual in several regards. Despite being bracketed by two chromitite layers, the pegmatoid itself typically contains little chromite. Where chromite is present, it generally occurs in the plagioclase-rich domains (Fig. 2). Large orthopyroxene grains appear to grow into the bounding chromite stringers as oikocrysts, seemingly causing undulations along the contact with the underlying chromitite (Figs. 2 and 5). The pegmatoid contains a higher modal abundance of sulphide than the bracketing chromitites, yet there are lesser amounts of resolvable PGM (Figs. 3 and 4). This is reflected by the generally lower PGE grades of this unit (Barnes and Maier, 2002). The anorthite contents of plagioclase are highly variable ($An_{40–70}$, present study and Hutchinson et al., 2015), possibly reflecting strong zonation consistent with closed-system intercumulus crystallisation.

In situ trace element data of orthopyroxene and plagioclase from RPM (unpublished data of the authors) indicate that most incompatible trace elements are slightly enriched relative to other rocks in the MR and show more variation, as previously shown by Mathez (1995) and Arndt et al. (2005). Yet, while some publications document higher whole-rock incompatible trace element contents of the pegmatoid than in hanging-wall pyroxenite (Hutchinson et al., 2015), others found no difference in composition between these rocks (Barnes and Maier, 2002; Cawthorn and Boerst, 2006). We conclude that the composition of the Merensky pegmatoid is likely more heterogenous than that of other UCZ rocks.

Barnes and Campbell (1988) proposed that the Merensky pegmatoid formed through increased diffusion rates due to higher water contents in a melt rich orthocumulate layer, whereas Barnes and Maier (2002) and Cawthorn and Boerst (2006) concluded that textural coarsening of a medium grained pyroxenite was caused by prolonged heating from magma being emplaced on top of the layer and ultimately forming the Merensky medium grained pyroxenite. However, this latter model fails to explain lenses of pegmatoid observed in the hanging-wall pyroxenite (Nicholson and Mathez, 1991). Such features could potentially be more readily explained by hydromagmatic models (Nicholson and Mathez, 1991; Boudreau, 1992), whereby the pegmatoid formed in response to hydration melting and consequent recrystallisation of a cumulate pile. We, and other authors (Roberts et al., 2007) found no evidence for anomalous abundances of hydrous phases (*i.e.,* amphibole, mica), but it could be argued that any volatiles were efficiently expelled from the cumulates during the final stages of crystallisation.

6.7. Medium-grained Merensky pyroxenite

The Merensky pyroxenite consists of subhedral orthopyroxene, with subhedral clinopyroxene and plagioclase oikocrysts. Orthopyroxene hosted in plagioclase oikocrysts are generally more Cr-rich and less clustered than those outside the oikocrysts. Sulphides (po > pn > ccp) are concentrated in the lowermost 5 cm of the unit and occur only in clustered orthopyroxene on the outside of plagioclase oikocrysts. Virtually no PGM are documented in the pyroxenite, which instead occur amongst sulphides (Fig. 3).

Euhedral to subhedral orthopyroxene preserved in plagioclase oikocrysts likely represents the original crystal-size distribution (CSD) of the orthopyroxene, whereas those outside underwent sintering and

annealing (loss of fines at the expense of larger crystals), causing their more irregular and clustered appearance. Sulphides do not occur as inclusions in orthopyroxene or plagioclase oikocrysts but interstitial to clustered orthopyroxene grains at the base of the interval. Godel et al. (2006) showed that MR sulphides are interconnected and form channelised networks, within which sulphide may efficiently percolate downward, whilst displacing residual liquid up (Barnes et al., 2017). Interaction between orthopyroxene and upward-displaced silicate liquid may explain the Cr-poor nature of the orthopyroxene with respect to that hosted in plagioclase oikocrysts.

Another important observation is that virtually no chromite is present in the pyroxenite. This is analogous to most other UCZ pyroxenites in the WBC (*e.g.*, Maier and Barnes, 2008), yet is markedly different from many LCZ and LZ pyroxenites which can be highly enriched in disseminated chromite (Teigler and Eales, 1996). This paucity of chromite in the Merensky pyroxenite is particularly notable since the pyroxenite is in direct contact to a chromite stringer, raising some doubt whether the Cr stringer could have formed *via* granular flow and kinetic sieving of Merensky pyroxenite. Experimental work of Barnes (1986) showed that chromite and orthopyroxene may co-precipitate under reducing conditions, whereas at higher fO_2, the distribution coefficient of chromite between orthopyroxene and the melt increases. The paucity of chromite in the Merensky pyroxenite could thus reflect elevated fO_2 relative to the LZ and LCZ pyroxenites.

7. Conclusions

The Merensky Reef (MR) of the Bushveld Complex is a highly unusual, mostly several dm-wide layer that has a strike-lengths of several 100 s of km. It comprises a pegmatoidal pyroxenite, bracketed by chromitite stringers, and underlain by an anorthosite interval. In the present paper we have studied Merensky Reef samples from several localities in the western Bushveld Complex and compiled several key observations that place added constraints on its formation:

(1) The contact between the footwall anorthosite and chromitite stringer is extremely sharp, with no obvious signs of mixing. Interaction between these units is mostly limited to the downward percolation of sulphide melt. The sulphides do not extend into the norite below the anorthosite, suggesting the norite had solidified prior to the percolation of sulphide.

(2) The base of the lower chromitite stringer is characterised by skeletal and amoeboidal chromite, whereas the remainder of the chromitite, and the upper chromitite, are characterised by equant and amoeboidal chromite. These textures are indicative of supercooling at the base of the lower chromitite stringer, and *in situ* growth.

(3) Sulphides occur in the footwall anorthosite, the chromitite stringers, the pegmatoid, the lowermost few centimeters of the medium grained hanging wall pyroxenite. There is little variation in modal abundance of bulk sulphides, and in relative modal proportions of individual sulphide phases between rock types. The co-occurrence of sulphide and phlogopite indicate sulphide melt co-existing with late-stage residual liquid, perhaps displacing it upward. The occurrence of sub-vertical sulphide channels in the footwall anorthosite lends support to a model of sulphide melt percolation.

(4) Pt-PGM are common in the reef lithologies but are virtually absent in the footwall and hanging-wall. The grains mostly occur at or just outside the edges of sulphides, suggesting recrystallisation.

Supplementary data to this article can be found online at https://doi.org/10.1016/j.gsf.2020.11.001.

Declaration of competing interest

The authors declare that they have no known competing financial interests or personal relationships that could have appeared to influence the work reported in this paper.

Acknowledgements

Dr. Duncan Muir is acknowledged for conducting SEM-EDS element mapping of sample NTH-10b, and Anthony Oldroyd for preparation of thin sections. Chris Ryan assisted with processing the Maia Mapper data. Yann Lahaye is thanked for conducting *in situ* Sr isotope analysis of plagioclase from the Karee specimen. Review comments from Ed Mathez and one anonymous reviewer greatly improved an earlier draft of this manuscript.

References

Abernethy, K.E., 2019. Assimilation of Dolomite by Bushveld Magmas in the Flatreef; Implications for the Origin of Ni-Cu-PGE Mineralization and the Precambrian Atmosphere. Ph.D. thesis. Cardiff University.

Arndt, N., Jenner, G., Ohnenstetter, M., Deloule, E., Wilson, A.H., 2005. Trace elements in the Merensky Reef and adjacent norites Bushveld complex South Africa. Mineral. Deposita 40 (5), 550–575.

Ballhaus, C.G., Stumpfl, E.F., 1986. Sulfide and platinum mineralization in the Merensky Reef: evidence from hydrous silicates and fluid inclusions. Contrib. Mineral. Petrol. 94 (2), 193–204.

Ballhaus, C.G., Cornelius, M., Stumpfl, E.F., 1988. The upper critical zone of the Bushveld Complex and the origin of merensky-type ores: a discussion. Econ. Geol. 83 (5), 1082–1085.

Barnes, S.J., 1986. The distribution of chromium among orthopyroxene, spinel and silicate liquid at atmospheric pressure. Geochim. Cosmochim. Acta 50 (9), 1889–1909.

Barnes, S.J., Campbell, I.H., 1988. Role of late magmatic fluids in Merensky-type platinum deposits: a discussion. Geology 16 (6), 488–491.

Barnes, S.-J., Maier, W.D., 2002. Platinum-group element distributions in the Rustenberg Layered Suite of the Bushveld Complex, South Africa. In: Cabri, L.J. (Ed.), The Geology, Geochemistry, Mineralogy and Mineral Beneficiation of Platinum-Group Elements. Canadian Institute of Mining, Metallurgy and Petroleum, Special Volume 54, pp. 431–458.

Barnes, S.J., Mungall, J.E., Le Vaillant, M., Godel, B., Lesher, C.M., Holwell, D., Lightfoot, P.C., Krivolutskaya, N., Wei, B., 2017. Sulfide-silicate textures in magmatic Ni-Cu-PGE sulfide ore deposits: disseminated and net-textured ores. Am. Mineral. 102 (3), 473–506.

Barry, J.A., 1964. Pothole and koppie investigation at Rustenburg Platinum Mines. Intern. Rep.(unpubl.). JCI, Johannesburg, p. 5.

Boudreau, A.E., 1988. Investigations of the Stillwater Complex; 4, The role of volatiles in the petrogenesis of the JM Reef, Minneapolis adit section. Can. Mineral. 26 (1), 193–208.

Boudreau, A., 1999. Fluid fluxing of cumulates: the JM reef and associated rocks of the Stillwater Complex, Montana. Journal of Petrology 40 (5), 755–772.

Boudreau, A.E., 1992. Volatile fluid overpressure in layered intrusions and the formation of potholes. Austr. J. Earth Sci. 39 (3), 277–287.

Boudreau, A.E., 2008. Modeling the Merensky Reef, Bushveld Complex, Republic of South Africa. Contrib. Mineral. Petrol. 156 (4), 431–437.

Boudreau, A.E., McCallum, I.S., 1992. Concentration of platinum-group elements by magmatic fluids in layered intrusions. Econ. Geol. 87 (7), 1830–1848.

Buntin, T.J., Grandstaff, D.E., Ulmer, G.C., Gold, D.P., 1985. A pilot study of geochemical and redox relationships between potholes and adjacent normal Merensky Reef of the Bushveld complex. Econ. Geol. 80 (4), 975–987.

Buthelezi, M., 2018. Significance of Liquid Inclusions in the COH Fluid System of the Upper Zone, Bushveld Igneous Complex. Ph.D thesis. University of the Witwatersrand, South Africa.

Campbell, I.H., 1986. A fluid dynamic model for the potholes of the Merensky Reef. Econ. Geol. 81 (5), 1118–1125.

Campbell, I.H., Naldrett, A.J., Barnes, S.J., 1983. A model for the origin of the platinum-rich sulfide horizons in the Bushveld and Stillwater Complexes. J. Petrol. 24 (2), 133–165.

Caricchi, L., Sheldrake, T.E., Blundy, J., 2018. Modulation of magmatic processes by CO_2 flushing. Earth Planet. Sci. Lett. 491, 160–171.

Carr, H.W., Kruger, F.J., Groves, D.I., Cawthorn, R.G., 1999. The petrogenesis of Merensky Reef potholes at the Western platinum Mine, Bushveld Complex: Sr-isotopic evidence for synmagmatic deformation. Mineral. Deposita 34 (4), 335–347.

Cawthorn, R.G., 2015. The Bushveld Complex, South Africa. Layered Intrusions. Springer, pp. 517–587 https://doi.org/10.1007/978-94-017-9652-1_12.

Cawthorn, R.G., Boerst, K., 2006. Origin of the pegmatitic pyroxenite in the Merensky unit, Bushveld Complex, South Africa. J. Petrol. 47 (8), 1509–1530.

Chistyakova, S., Latypov, R., Youlton, K., 2019. Multiple Merensky Reef of the Bushveld Complex, South Africa. Contrib. Mineral. Petrol. 174 (3), 26.

Cox, D.P., Singer, D.A., 1986. Mineral Deposit Models. Vol. 1693. Bulletin: US Government Printing Office.

Eales, H.V., Cawthorn, R.G., 1996. The Bushveld Complex. Developments in Petrology, Vol. 15. Elsevier, pp. 181–229.

Eales, H.V., Reynolds, I.M., 1986. Cryptic variations within chromitites of the upper critical zone, northwestern Bushveld complex. Econ. Geol. 81 (5), 1056–1066.

Eales, H.V., Marsh, J.S., Mitchell, A.A., De Klerk, W.J., Kruger, F.J., Field, M., 1986. Some geochemical constraints upon models for the crystallization of the upper critical zone-main zone interval, northwestern Bushveld complex. Mineral. Mag. 50 (358), 567–582.

Eales, H.V., Field, M., De Klerk, W.J., Scoon, R.N., 1988. Regional trends of chemical variation and thermal erosion in the Upper Critical Zone, western Bushveld Complex. Mineral. Mag. 52 (364), 63–79.
Eales, H.V., De Klerk, W.J., Butcher, A.R., 1990. The cyclic unit beneath the UG1 chromitite (UGIFW unit) at RPM Union Section Platinum Mine—Rosetta Stone of the Bushveld Upper Critical Zone? Mineral. Mag. 54 (374), 23–43.
Forien, M., Tremblay, J., Barnes, S.J., Burgisser, A., Page, P., 2015. The role of viscous particle segregation in forming chromite layers from slumped crystal slurries: insights from analogue experiments. J. Petrol. 56 (12), 2425–2444.
Godel, B., Barnes, S.J., Maier, W.D., 2006. 3-D distribution of sulphide minerals in the Merensky Reef (Bushveld Complex, South Africa) and the JM Reef (Stillwater Complex, USA) and their relationship to microstructures using X-ray computed tomography. J. Petrol. 47 (9), 1853–1872.
Godel, B., Barnes, S.J., Maier, W.D., 2011. Parental magma composition inferred from trace element in cumulus and intercumulus silicate minerals: an example from the lower and lower critical zones of the Bushveld complex, South-Africa. Lithos 125 (1–2), 537–552.
Grobler, D.F., Brits, J.A.N., Maier, W.D., Crossingham, A., 2019. Litho- and chemostratigraphy of the Flatreef PGE deposit, northern Bushveld Complex. Mineral. Deposita 54 (1), 3–28.
Hall, A.L., 1924. On "jade" (massive garnet) from the Bushveld in the Western Transvaal. S. Afr. J. Geol. 27, 49–55.
Holness, M.B., Cawthorn, R.G., Roberts, J., 2017. The thickness of the crystal mush on the floor of the Bushveld magma chamber. Contrib. Mineral. Petrol. 172 (11—12), 102.
Hunt, E.J., Latypov, R., Horváth, P., 2018. The Merensky Cyclic Unit, Bushveld Complex, South Africa: reality or myth? Minerals 8 (4), 144.
Hutchinson, D., Foster, J., Prichard, H., Gilbert, S., 2015. Concentration of particulate platinum-group minerals during magma emplacement; a case study from the Merensky Reef, Bushveld Complex. J. Petrol. 56 (1), 113–159.
Hywel, I., 2015. On the Origin of the Merensky Footwall Anorthosite. M.S. thesis. Cardiff University, p. 71.
Irvine, T.N., Keith, D.W., Todd, S.G., 1983. The JM platinum palladium reef: H Origin by double-diffusive convective magma mixing and implications for the Bushveld complex. Econ. Geol. 78, 1287–1334.
Ivanic, T.J., Nebel, O., Jourdan, F., Faure, K., Kirkland, C.L., Belousova, E.A., 2015. Heterogeneously hydrated mantle beneath the late Archean Yilgarn Craton. Lithos 238, 76–85.
Jones, J.P., 1976. Pegmatoidal nodules in the layered rocks of the Bafokeng leasehold area. S. Afr. J. Geol. 79 (3), 312–320.
Karykowski, B.T., Yang, S.H., Maier, W.D., Lahaye, Y., Lissenberg, C.J., O'Brien, H., 2017. In situ Sr isotope compositions of plagioclase from a complete stratigraphic profile of the Bushveld complex, South Africa: evidence for extensive magma mixing and percolation. J. Petrol. 58 (11), 2285–2308.
Kinloch, E.D., 1982. Regional trends in the platinum-group mineralogy of the critical zone of the Bushveld complex, South Africa. Econ. Geol. 77 (6), 1328–1347.
Kirkham, R., Dunn, P.A., Kuczewski, A.J., Siddons, D.P., Dodanwela, R., Moorhead, G.F., Ryan, C.G., De Geronimo, G., Beuttenmuller, R., Pinelli, D., Pfeffer, M., 2010. The Maia spectroscopy detector system: engineering for integrated pulse capture, low-latency scanning and real-time processing. AIP Conference Proceedings. American Institute of Physics, 1234(1), pp. 240–243.
Kokh, M.A., Akinfiev, N.N., Pokrovski, G.S., Salvi, S., Guillaume, D., 2017. The role of carbon dioxide in the transport and fractionation of metals by geological fluids. Geochim. Cosmochim. Acta 197, 433–466.
Komar, P.D., 1972. Mechanical interactions of phenocrysts and flow differentiation of igneous dikes and sills. Geol. Soc. Am. Bull. 83 (4), 973–988.
Larsson, D.H., Takman, P.A., Lundström, U., Burvall, A., Hertz, H.M., 2011. A 24 keV liquid-metal-jet x-ray source for biomedical applications. Review of Scientific Instruments 82 (12), 123701.
Latypov, R.M., Chistyakova, S.Y., Namur, O., Barnes, S., 2020. Dynamics of evolving magma chambers: textural and chemical evolution of cumulates at the arrival of new liquidus phases. Earth-Science Reviews 210, 103388.
Latypov, R., Chistyakova, S., Page, A., Hornsey, R., 2015. The Merensky Reef of the Bushveld complex: origin by in situ crystallization from a basal layer of magma. J. Petrol. 56, 2341–2372.
Latypov, R., Chistyakova, S., Barnes, S.J., Hunt, E.J., 2017a. Origin of platinum deposits in layered intrusions by in situ crystallization: evidence from undercutting Merensky Reef of the Bushveld complex. J. Petrol. 58 (4), 715–761.
Lee, C.A., 1996. A review of mineralization in the Bushveld Complex and some other layered intrusions. Developments in Petrology, Vol 15. Elsevier, pp. 103–145.
Lee, C.A., Butcher, A.R., 1990. Cyclicity in the Sr isotope stratigraphy through the Merensky and Bastard Reef units, Atok section, eastern Bushveld complex. Econ. Geol. 85 (4), 877–883.
Leeb-Du Toit, A., 1986. The impala platinum mines. In: Anhaeusser, C.R., Maske, S. (Eds.), Mineral Deposits of Southern Africa. Geological Society of South Africa, Johannesburg, pp. 1091–1106.
Li, C., Ripley, E.M., Sarkar, A., Shin, D., Maier, W.D., 2005. Origin of phlogopite-orthopyroxene inclusions in chromites from the Merensky Reef of the Bushveld complex, South Africa. Contrib. Mineral. Petrol. 150 (1), 119–130.
Maier, W., 1995. Olivine oikocrysts in Bushveld Anorthosite; some implications for cumulate formation. Can. Mineral. 33 (5), 1011–1022.
Maier, W.D., Barnes, S.J., 2003. Platinum-group elements in the Boulder Bed, western Bushveld Complex, South Africa. Mineral. Deposita 38 (3), 370–380.
Maier, W., Barnes, S.J., 2008. Platinum-group elements in the UG1 and UG2 chromitites, and the Bastard reef, at Impala platinum mine, western Bushveld Complex, South Africa: evidence for late magmatic cumulate instability and reef constitution. S. Afr. J. Geol. 111 (2–3), 159–176.
Maier, W.D., Eales, H.V., 1997. Correlation within the UG2-Merensky Reef interval of the Western Bushveld Complex, based on geochemical, mineralogical and petrological data. Geological Survey of South Africa, Council for Geoscience, Vol. 120.
Maier, W.D., Teigler, B., 1995. A facies model for the western Bushveld complex. Econ. Geol. 90 (8), 2343–2349.
Maier, W.D., Barnes, S.J., Groves, D.I., 2013. The Bushveld complex, South Africa: formation of platinum–palladium, chrome-and vanadium-rich layers via hydrodynamic sorting of a mobilized cumulate slurry in a large, relatively slowly cooling, subsiding magma chamber. Mineral. Deposita 48 (1), 1–56.
Maier, W.D., Karykowski, B.T., Yang, S.H., 2016. Formation of transgressive anorthosite seams in the Bushveld complex via tectonically induced mobilisation of plagioclase-rich crystal mushes. Geosci. Front. 7 (6), 875–889.
Marsh, B.D., 2013. On some fundamentals of igneous petrology. Contrib. Mineral. Petrol. 166 (3), 665–690.
Schmincke, H.U., 1967. Fused tuff and pépérites in south-central Washington. Geol. Soc. Am. Bull. 78, 319–330. https://doi.org/10.1130/0016-7606(1967)78[319:FTAPIS]2.0.CO;2.
Mathez, E.A., Kinzler, R.J., 2017. Metasomatic chromitite seams in the Bushveld and Rum Layered intrusions. Elements 13 (6), 397–402.
Mathez, E.A., Mey, J.L., 2005. Character of the UG2 chromitite and host rocks and petrogenesis of its pegmatoidal footwall, northeastern Bushveld complex. Econ. Geol. 100 (8), 1617–1630.
Mathez, E.A., Dietrich, V.J., Holloway, J.R., Boudreau, A.E., 1989. Carbon distribution in the stiliwater complex and evolution of vapor during crystallization of Stillwater and Bushveld magmas. J. Petrol. 30 (1), 153–173.
Mathez, E.A., Hunter, R.H., Kinzler, R., 1997. Petrologic evolution of partially molten cumulate: the Atok section of the Bushveld complex. Contrib. Mineral. Petrol. 129 (1), 20–34.
McBirney, A.R., Sonnenthal, E.L., 1990. Metasomatic replacement in the Skaergaard Intrusion, East Greenland: preliminary observations. Chem. Geol. 88 (3–4), 245–260.
Mitchell, A.A., Scoon, R.N., 2007. The Merensky Reef at Winnaarshoek, Eastern Bushveld Complex: a primary magmatic hypothesis based on a wide reef facies. Econ. Geol. 102 (5), 971–1009.
Mitchell, A.A., Henckel, J., Mason-Apps, A., 2019. The Upper critical Zone of the Rustenburg Layered Suite in the Swartklip Sector, north-western Bushveld Complex, on the farm Wilgerspruit 2JQ: I. Stratigraphy and PGE mineralization patterns. S. Afr. J. Geol. 122 (2), 117–142.
Mungall, J.E., Kamo, S.L., McQuade, S., 2016. U–Pb geochronology documents out-of-sequence emplacement of ultramafic layers in the Bushveld Igneous Complex of South Africa. Nat. Commun. 7 (1), 1–13.
Naldrett, A.J., Gasparrini, E.C., Barnes, S.J., Von Gruenewaldt, G., Sharpe, M.R., 1986. The Upper critical Zone of the Bushveld Complex and the origin of Merensky-type ores. Econ. Geol. 81 (5), 1105–1117.
Naldrett, A.J., Cameron, G., Von Gruenewaldt, G., Sharpe, M.R., 1987. The formation of stratiform PGE deposits in layered intrusions. In: Parson, I. (Ed.), Origins of Igneous Layering. NATO ASI Series (Series C: Mathematical and Physical Sciences), Vol. 196. Springer, Dordrecht, pp. 313–397.
Naldrett, A.J., Lehmann, J., 1988. Spinel non-stoichiometry as the explanation for Ni-, Cu- and PGE-enriched sulphides in chromitites. In: Prichard, H.M., Potts, P.J., Bowles, J.S.W., Cribb, S.J. (Eds.), Geo-Platinum, Vol. 87. Springer, Dordrecht, pp. 93–109 https://doi.org/10.1007/978-94-009-1353-0_10.
Naldrett, A.J., Wilson, A., Kinnaird, J., Chunnett, G., 2009. PGE tenor and metal ratios within and below the Merensky Reef, Bushveld Complex: implications for its genesis. J. Petrol. 50 (4), 625–659.
Nicholson, D.M., Mathez, E.A., 1991. Petrogenesis of the Merensky Reef in the Rustenburg section of the Bushveld complex. Contrib. Mineral. Petrol. 107 (3), 293–309.
Raedeke, L.D., McCallum, I.S., 1984. Investigations in the Stillwater complex: Part II. Petrology and petrogenesis of the ultramafic series. J. Petrol. 25 (2), 395–420.
Roberts, M.D., Reid, D.L., Miller, J.A., Basson, I.J., Roberts, M., Smith, D., 2007. The Merensky Cyclic Unit and its impact on footwall cumulates below Normal and Regional Pothole reef types in the Western Bushveld Complex. Mineral. Deposita 42 (3), 271–292.
Ryan, C.G., Kirkham, R., Hough, R.M., Moorhead, G., Siddons, D.P., De Jonge, M.D., Paterson, D.J., De Geronimo, G., Howard, D.L., Cleverley, J.S., 2010. Elemental X-ray imaging using the Maia detector array: the benefits and challenges of large solid-angle. Nucl. Instrum. Methods Phys. Res. Sect. A: Accel. Spectrometers Detect. Associated Equip. 619 (1–3), 37–43.
Ryan, C.G., Siddons, D.P., Kirkham, R., Li, Z.Y., De Jonge, M.D., Paterson, D.J., Kuczewski, A., Howard, D.L., Dunn, P.A., Falkenberg, G., Boesenberg, U., 2014. Maia X-ray fluorescence imaging: Capturing detail in complex natural samples. J. Phys. Conf. Ser. 499 (1), 012002.
Ryan, C.G., Kirkham, R., Moorhead, G.F., Parry, D., Jensen, M., Faulks, A., Hogan, S., Dunn, P.A., Dodanwela, R., Fisher, L.A., Pearce, M., 2018. Maia Mapper: high definition XRF imaging in the lab. J. Instrum. 13 (03), C03020.
Schmidt, E.R., 1952. The structure and composition of the Merensky Reef and associated rocks on the Rustenburg platinum mine. S. Afr. J. Geol. 55 (1), 233–279.
Scoates, J.S., Wall, C.J., 2015. Geochronology of layered intrusions. In: Charlier, B., Namur, O., Latypov, R., Tegner, C. (Eds.), Layered Intrusions. Springer Geology. Springer, Dordrecht, pp. 3–74.
Scoates, J.S., Lindsley, D.H., Frost, B.R., 2010. Magmatic and structural evolution of an anorthositic magma chamber: the Poe Mountain intrusion, Laramie anorthosite complex, Wyoming. Can. Mineral. 48 (4), 851–885.
Sonnenthal, E.L., 1992. Geochemistry of dendritic anorthosites and associated pegmatites in the Skaergaard Intrusion, East Greenland: evidence for metasomatism by a chlorine-rich fluid. J. Volcanol. Geotherm. Res. 52 (1–3), 209–230.

Tanner, D., Mavrogenes, J.A., Arculus, R.J., Jenner, F.E., 2014. Trace element stratigraphy of the Bellevue Core, Northern Bushveld: multiple magma injections obscured by diffusive processes. J. Petrol. 55 (5), 859–882.
Teigler, B., Eales, H.V., 1996. The Lower and Critical Zones of the western limb of the Bushveld Complex as intersected by the Nooitgedacht boreholes. Geological Survey of South Africa, Council for Geoscience, pp. 111–112.
Vermaak, C.F., 1976. The Merensky Reef; thoughts on its environment and genesis. Econ. Geol. 71 (7), 1270–1298.
Viljoen, M.J., 1999. The nature and origin of the Merensky Reef of the western Bushveld complex based on geological facies and geophysical data. S. Afr. J. Geol. 102 (3), 221–239.
Viljoen, M.J., De Klerk, W.J., Coetzer, P.M., Hatch, N.P., Kinloch, E., 1986. The union section of Rustenburg Platinum Mines Limited, with reference to the Merensky Reef. In: Anhaeusser, C.R., Maske, S. (Eds.), Mineral Deposits of Southern Africa. Geol. Soc. South Africa, Johannesburg, pp. 1060–1090.
Viljoen, M.J., Hieber, R., 1986. The Rustenburg section of Rustenburg Platinum Mines Limited, with reference to the Merensky reef. In: Anhaeusser, C.R., Maske, S. (Eds.), Mineral Deposits of Southern Africa. Geological Society of South Africa, Johannesburg, pp. 1107–1134.
Von Gruenewaldt, G., 1979. A review of some recent concepts of the Bushveld Complex, with particular reference to sulfide mineralization. Can. Mineral. 17 (2), 233–256.
Vukmanovic, Z., Barnes, S.J., Reddy, S.M., Godel, B., Fiorentini, M.L., 2013. Morphology and microstructure of chromite crystals in chromitites from the Merensky Reef (Bushveld Complex, South Africa). Contrib. Mineral. Petrol. 165 (6), 1031–1050.
Wagner, P.A., 1929. The Platinum Deposits and Mines of South Africa. Oliver and Boyd, Edinburgh and London, p. 326.
Wallmach, T., Hatton, C.J., De Waal, S.A., Gibson, R.L., 1995. Retrogressive hydration of calc-silicate xenoliths in the eastern Bushveld complex: evidence for late magmatic fluid movement. J. Afr. Earth Sci. 21 (4), 633–646.
Wilson, A.H., Lee, C.A., Brown, R.T., 1999. Geochemistry of the Merensky reef, Rustenburg Section, Bushveld complex: controls on the silicate framework and distribution of traceelements. Mineral. Deposita 34 (7), 657–672.
Yang, S.H., Maier, W.D., Lahaye, Y., O'Brien, H., 2013. Strontium isotope disequilibrium of plagioclase in the Upper critical Zone of the Bushveld complex: evidence for mixing of crystal slurries. Contrib. Mineral. Petrol. 166 (4), 959–974.